J. Fluid Mech. (1986), *vol.* 169, *pp.* 173–210
Printed in Great Britain

Natural convection in an enclosed vertical air layer with large horizontal temperature differences

By D. R. CHENOWETH AND S. PAOLUCCI
Applied Mechanics Department, Sandia National Laboratories, Livermore, CA 94550, USA

(Received 29 July 1985 and in revised form 30 January 1986)

Steady-state two-dimensional results obtained from numerical solutions to the transient Navier-Stokes equations are given for laminar convective motion of a gas in an enclosed vertical slot with large horizontal temperature differences. We present results for air using the ideal-gas law and Sutherland-law transport properties, although the results are also valid for hydrogen. Wide ranges of aspect-ratio, Rayleigh-number and temperature-difference parameters are examined. The results are compared in detail with the exact solution in the conduction and fully developed merged boundary-layer limits for arbitrary temperature difference, and to the well-established Boussinesq limit for small temperature difference. It is found that the static pressure, and temperature and velocity distributions are very sensitive to property variations, even though the average heat flux is not. In addition we observe a net vertical heat flux to be the same as that obtained from the Boussinesq equations. We concentrate on the boundary-layer regime, but we present a rather complete picture of different flow regimes in Rayleigh-number, aspect-ratio and temperature-difference parameter space. We observe that, with increasing temperature difference, lower critical Rayleigh numbers for stationary and oscillatory instabilities are obtained. In addition we observe that in some cases the physical nature of the instability changes with increasing temperature difference.

1. Introduction

Although gas gaps between vertical parallel walls have been used for many decades to reduce heat transfer, their use with large horizontal temperature differences has become increasingly important during the last two decades. Examples of typical applications include insulation using double-pane windows or double walls, nuclear reactors, fire within buildings, solar collectors, and electronic components in enclosures. Still, the majority of the published investigations involve small temperature differences where gas properties are taken to be constant and the Boussinesq limiting equations are valid. Some of the known non-Boussinesq analytical and experimental results are briefly discussed here prior to describing our current numerical solutions.

Hara (1958), and Sparrow & Gregg (1958) gave analytical results for a vertical flat plate with large temperature differences. In general their results are not applicable to the vertical slot; however, we will show how the heat transfer results can be adapted to our problem. Polezhaev (1967) used equal Sutherland laws for dynamic viscosity μ and thermal conductivity k (constant Prandtl number when the heat capacity at constant pressure is constant) in his numerical solution of the compressible Navier–Stokes equations; he used a relatively small temperature-difference parameter

of $\epsilon = 0.2$ and slot aspect ratios of unity. Here ϵ is defined as the difference between the hot and cold wall temperatures divided by their sum. Rubel & Landis (1970) made an expansion in terms of ϵ to obtain first-order corrections to the zeroth-order Boussinesq results. Rubel & Landis included fluid property variations by means of temperature power-law expressions and they assumed that the pressure was independent of the temperature difference as well as other parameters. Leonardi & Reizes (1979, 1981) also numerically solved the compressible Navier–Stokes equations using equal Sutherland laws for μ and k; however, they did examine cases where larger temperature differences were involved ($\epsilon \leqslant 0.6$), and they studied only aspect ratios of 1 and 2, although some of their results, as will be discussed later, are suspect.

Experimental studies using gases with large temperature differences have been equally sparse. Eckert & Carlson (1961) did investigate the high-aspect-ratio problem, but they only examined cases where $\epsilon \leqslant 0.13$, so that the Boussinesq solution is approximately valid for their results. Similarly, all of the Mordchelles-Regnier & Kaplan (1963) experiments in the laminar region were in the Boussinesq regime, although they did obtain some turbulent non-Boussinesq results for a single flat plate. More recently, Duxbury (1979) obtained experimental results covering a wide parameter range in the steady laminar regime, but with $\epsilon \leqslant 0.15$. It is not clear to what extent the above experimental studies were affected by heat losses from the ends.

Chenoweth & Paolucci (1985) investigated the steady-state fully developed boundary-layer region for large temperature differences between vertical isothermal walls. They derived some exact laminar solutions to the Navier–Stokes equations for perfect gases with the properties described by unequal Sutherland laws. They produced variable Prandtl-number results for $0 < \epsilon < 1.0$ using air as an example, although the accuracy of the Sutherland-law conductivity degrades rapidly above $\epsilon = 0.6$. This paper also uses unequal Sutherland-law transport properties and a perfect gas equation of state to produce large temperature difference results for air. Numerical solutions of the transient Navier–Stokes equations are used to generate laminar steady-state results primarily in the independent boundary-layer region and the developing merged boundary-layer region. However, other flow regions are also covered to the extent necessary to construct a better understanding of the entire laminar parameter range for all aspect ratios greater than or equal to unity. We point out that the need to construct a map of flow regions in parameter space, which includes stationary and oscillatory stability boundaries, necessitated the use of the transient form of the equations.

In §§2 to 4 we present the governing equations and outline the algorithm for their numerical solution. We follow in §5 with a discussion of the different flow regions possible in this problem. In §6, expressions for pressure and heat flux are derived from constraints of the problem. An extensive validation of the computer program is reported in §7. Finally, in §8, we present non-Boussinesq results in the boundary-layer region, and conclude in §9 by comparing our results with those of others.

2. Governing equations

Consider a two-dimensional rectangular enclosure of width L and height H which contains a gas. The gas is initially quiescent at a uniform temperature T_0 and pressure p_0. The walls of the vessel are initially at the same temperature T_0. At times larger than zero, the left and right walls are maintained at temperatures of T_h and T_c,

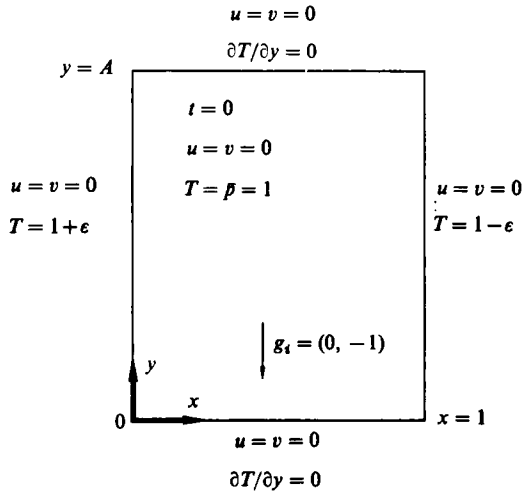

FIGURE 1. Problem definition.

respectively, where $T_h > T_c$. The top and bottom walls are insulated. The above problem is illustrated in figure 1, where we have used the following non-dimensionalizations (starred quantities are dimensional):

$$\left.\begin{gathered} x_i^* = Lx_i, \quad t^* = \frac{L}{U}t, \quad v_i^* = Uv_i, \\ \bar{p}^* = p_0\bar{p}, \quad T^* = T_0T, \quad \rho^* = \rho_0\rho, \quad \Pi^* = \rho_0 U^2\Pi, \\ \mu^* = \mu_0\mu, \quad k^* = k_0k, \quad c_p^* = c_{p_0}c_p. \end{gathered}\right\} \tag{2.1}$$

The independent dimensionless parameters appearing in the problem are

$$\left.\begin{gathered} A = \frac{H}{L}, \quad \epsilon = \frac{\Delta T}{2T_0}, \quad \gamma = \frac{c_{p_0}}{c_{v_0}}, \\ Pr = \frac{\nu_0}{\alpha_0}, \quad Ra = \frac{2\epsilon g L^3}{\nu_0\alpha_0}, \quad Ma = \frac{U}{c_0}. \end{gathered}\right\} \tag{2.2}$$

In (2.1)–(2.2), zero subscripts denote the initial dimensional values; the reference speed U is defined to be the thermal diffusion speed, i.e. $U = \alpha_0/L$; ν_0 and α_0 are the kinematic viscosity and thermal diffusivity, respectively, while μ_0 and k_0 are the dynamic viscosity and thermal conductivity respectively; p_0 is the pressure; c_0 is the sound speed; c_{p_0} and c_{v_0} are the specific heats at constant pressure and volume, respectively; and lastly g is the magnitude of the gravitational field. Note that $\Delta T = T_h - T_c$ and we choose T_h and T_c such that $T_0 = \frac{1}{2}(T_h + T_c)$. The dimensionless parameters in (2.2) are the aspect ratio, the wall temperatures differential, the ratio of specific heats, the Prandtl number, the Rayleigh number and the Mach number respectively.

The problem evolves in time t and can be described in terms of the velocity components $v_i = (u, v)$ in the $x_i = (x, y)$ directions, the density ρ, temperature T, and pressure p. The governing equations are statements of conservation of mass, momentum and energy, with the addition of a state equation describing the gas. These

equations, valid under a small-Mach-number approximation, have been derived by Paolucci (1982) and are given as follows:

$$\frac{\partial \rho}{\partial t}+\frac{\partial \rho v_j}{\partial x_j}=0, \tag{2.3}$$

$$\frac{\partial \rho v_i}{\partial t}+\frac{\partial}{\partial x_j}(\rho v_j v_i)=-\frac{\partial \Pi}{\partial x_i}+\frac{Ra\,Pr}{2\epsilon}\rho n_i+Pr\frac{\partial}{\partial x_j}\tau_{ij}, \tag{2.4}$$

$$\rho c_p\left(\frac{\partial T}{\partial t}+v_j\frac{\partial T}{\partial x_j}\right)-\Gamma\frac{\mathrm{d}\bar{p}}{\mathrm{d}t}=\frac{\partial}{\partial x_j}\left(k\frac{\partial T}{\partial x_j}\right), \tag{2.5}$$

$$\rho=\rho(\bar{p},T), \tag{2.6}$$

where $\Pi=p^{(1)}/(\gamma Ma^2)$ is a reduced pressure which accounts for the hydrostatic and dynamic effects, $p^{(1)}$ is the second term in the Mach number expansion of p and is $O(Ma^2)$, n_i is the unit vector in the direction of gravity, τ_{ij} is the viscous stress tensor given by

$$\tau_{ij}=\mu\left(\frac{\partial v_i}{\partial x_j}+\frac{\partial v_j}{\partial x_i}\right)-\frac{2}{3}\delta_{ij}\mu\frac{\partial v_k}{\partial x_k}, \tag{2.7}$$

δ_{ij} is the Kronecker delta function, and $\Gamma=(\gamma-1)/\gamma$ is a measure of the resilience of the fluid. The thermal conductivity, viscosity and specific heat at constant pressure are functions of the thermodynamic variables. Note that the Mach number only serves as a scaling for the dynamic and hydrostatic components of pressure, and Γ only enters in the transient solution.

The initial and boundary conditions expressed in dimensionless form are (see figure 1):

$$v_i(x_j,0)=0, \quad \bar{p}(0)=1, \quad T(x_j,0)=1, \tag{2.8}$$

$$\left.\begin{aligned} &v_i(0,y,t)=v_i(1,y,t)=v_i(x,0,t)=v_i(x,A,t)=0,\\ &T(0,y,t)=1+\epsilon, \quad T(1,y,t)=1-\epsilon, \quad \frac{\partial T}{\partial y}(x,0,t)=\frac{\partial T}{\partial y}(x,A,t)=0. \end{aligned}\right\} \tag{2.9}$$

The spatially uniform pressure $\bar{p}=p^{(0)}(t)$ appearing in the energy equation and the equation of state, which represents the first term in the expansion of p, accounts for the change of the static pressure with time. The separation of the pressure components, holding under the small-Mach-number approximation, is the essence of the acoustic waves 'filtering' (Paolucci 1982); however, this splitting introduces $\bar{p}$ as an extra unknown. It can be shown that the equation for $\bar{p}$, obtained by a global mass conservation statement and the use of boundary conditions, is given by

$$\frac{\mathrm{d}}{\mathrm{d}t}\int_V \exp\left[-\int_1^T \beta\,\mathrm{d}T'+\int_1^{\bar{p}}\kappa\,\mathrm{d}p'\right]\mathrm{d}V=0, \tag{2.10}$$

where V is the volume of the cavity, $\beta=-(\partial\rho/\partial T)_{\bar{p}}/\rho$ is the coefficient of volume expansion, and $\kappa=(\partial\rho/\partial\bar{p})_T/\rho$ is the isothermal compressibility coefficient.

If we let

$$D=\frac{\partial}{\partial x_i}(\rho v_i), \tag{2.11}$$

then it can be shown that the continuity equation (2.3) is identically satisfied if the pressure component Π is obtained from the following elliptic equation

$$\frac{\partial^2 \Pi}{\partial x_i\,\partial x_i}=\frac{\partial}{\partial x_i}R_i-\frac{\partial}{\partial t}D, \tag{2.12}$$

where
$$R_i = -\frac{\partial}{\partial x_j}(\rho v_j v_i) + Pr\frac{\partial}{\partial x_j}\tau_{ij} + \frac{Ra\,Pr}{2\epsilon}\rho n_i, \tag{2.13}$$

$$D = \frac{1}{c_p T}\left[-\rho c_p v_j \frac{\partial T}{\partial x_j} + (\Gamma - c_p)\frac{d\bar{p}}{dt} + \frac{\partial}{\partial x_j}\left(k\frac{\partial T}{\partial x_j}\right)\right]. \tag{2.14}$$

3. Relations between state variables and transport properties

For a real gas, the equation of state is

$$\bar{p} = Z\rho T, \tag{3.1}$$

where Z is the compressibility factor normalized by its initial value; then (2.10) can be rewritten for this special case as

$$\frac{d\bar{p}}{dt} = \frac{1}{\int_V (c_p/Z - \Gamma)\,dV}\left[\int_S k\frac{\partial T}{\partial x_j}dS_j + \bar{p}\int_V \left(\frac{c_p}{Z^2}\frac{\partial Z}{\partial t} + \frac{v_j}{Z}\frac{\partial c_p}{\partial x_j}\right)dV\right], \tag{3.2}$$

where V and S denote the volume and surface of the cavity respectively. Note that with (3.2) the energy equation (2.5) is an integro-differential equation.

In this paper we only present results for an ideal diatomic gas ($Z = 1, c_p = 1, \gamma = \frac{7}{5}$) with a reference Prandtl number $Pr = 0.71$. The dimensionless thermal conductivity and viscosity are obtained using the Sutherland law forms

$$k = \frac{T^{\frac{3}{2}}(1 + S_k)}{(T + S_k)}, \tag{3.3}$$

$$\mu = \frac{T^{\frac{3}{2}}(1 + S_\mu)}{(T + S_\mu)}, \tag{3.4}$$

where White (1974) gives the dimensional values of $S^* = ST_0$ for viscosity and conductivity for a variety of gases along with their corresponding ranges of validity. Although the local Prandtl number is constant when $S_k = S_\mu$ and the specific heat at constant pressure is constant, this simplification is not justified in many cases.

Here we use dimensionless S values of $S_\mu = 0.368$ and $S_k = 0.648$ (local Prandtl number not constant). As an example, when $T_0 = 300$ °K, $T_h = 480$ °K and $T_c = 120$ °K ($\epsilon = 0.6$), for air (Hilsenrath *et al.* 1960) the maximum viscosity error for the entire temperature range is less than 1 %, that for c_p is approximately 2 % (at the hot wall), and the maximum error in k is near -6 % (at the cold wall). Equation (3.3) for air degrades rapidly above $\epsilon = 0.6$.

It is interesting to note that the steady-state results given here apply as well to gases other than air, although the temperature range may be somewhat different. For example, at a reference temperature of 260 °K, hydrogen has a reference Prandtl number of 0.70, and $S_\mu = 0.372$ and $S_k = 0.641$, so that the results should be approximately the same as those for air, but for different values of L, H and ΔT.

4. Numerical algorithm

4.1. *The computational mesh*

The physical domain is discretized in the (x, y)-plane using three uniform interlacing meshes as shown schematically in figure 2. Through using an interlacing grid system, the amount of averaging to obtain values of variables at locations where they are not defined is reduced to a minimum, thus improving accuracy. Furthermore, this

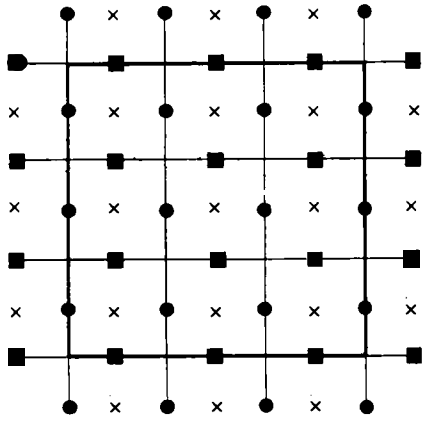

FIGURE 2. Schematic structure of the discretized region in the (x, y)-plane for the horizontal velocity u (●), the vertical velocity v (■), and all scalar variables (×). Thick full lines denote the boundaries of the rectangular region at $x = 0, 1$ (vertical lines) and $y = 0, A$ (horizontal lines).

lattice structure enforces correct momentum balance of the discretized equations for every momentum cell, and the continuity equation has a unique exact form which can only be achieved by such a grid; this uniqueness is essential for deriving the discretized form of the Poisson equation (2.12).

The positions of the grid points and their spacings are chosen such that the fluid boundaries lie halfway between scalar points (×). Thus the top and bottom boundaries go through v points (■), and the vertical boundaries go through u points (●). Note that there is one layer of grid points outside the region of interest, as indicated in figure 2, to facilitate the application of boundary conditions.

4.2. *The numerical procedure*

We have solved (2.4), (2.5), (2.7), (2.12)–(2.14), and (3.1)–(3.4) on this staggered grid with an explicit predictor–corrector finite-difference method using forward differences for time derivatives and central differences for spatial derivatives, with a truncation error $O(\Delta t, \Delta x^2)$. The computational procedure is as follows:

1. Velocity and scalar fields are known at time t^n.
2. Compute stable integration step Δt^n and advance time to t^{n+1}.
3. Obtain $\mathrm{d}\bar{p}(t^n)/\mathrm{d}t$ and predicted pressure $\bar{p}^+$ from (3.2).
4. Solve, in order, for predicted density ρ^+ from (3.1), reduced pressure Π^+ from (2.12), and momentum fluxes $(\rho v_i)^+$ from (2.4).
5. Using current values, obtain a corrected reduced pressure Π^{n+1} from (2.12) and subsequently the momentum fluxes $(\rho v_i)^{n+1}$ from (2.4).
6. The discretized energy equation (2.5) is integrated in conservative form to obtain T^{n+1}.
7. From $\bar{p}^+$ correct the static pressure $\bar{p}^{n+1}$ by eliminating any global mass imbalance, and subsequently obtain the corrected density ρ^{n+1} from (3.1).
8. The velocity components are now calculated from $v_i^{n+1} = (\rho v_i)^{n+1}/\rho^{n+1}$.
9. Properties are re-evaluated to reflect current thermodynamic conditions.
10. The process is repeated for the next integration step.

A few comments are in order regarding the above procedure. A stable integration timestep is obtained from

$$\Delta t \leqslant \tfrac{1}{2} \max_{i,j} \left(\frac{k}{\rho c_p}, Pr \frac{\mu}{\rho} \right) \left(\frac{1}{\Delta x^2} + \frac{1}{\Delta y^2} \right), \tag{4.1}$$

and
$$\Delta t \leqslant 2 \min_{i,j} \left(\frac{k}{\rho c_p}, Pr \frac{\mu}{\rho} \right) / (u^2 + v^2), \tag{4.2}$$

where the maximum and minimum in (4.1) and (4.2) are obtained over all the grid points interior to the computational region. For a single, linear, constant-property, convection–diffusion equation with no source term and with diffusion coefficient α, the stability restrictions are exactly given by (4.1) and (4.2), with α replacing the maximum and minimum in the two equations respectively (see Hindmarsh, Gresho & Griffiths 1984). Then, it can be shown that (4.1) is more restrictive when both $|u|\Delta x/\alpha, |v|\Delta y/\alpha < 4$, while (4.2) is more restrictive if both $|u|\Delta x/\alpha, |v|\Delta y/\alpha > 4$. Otherwise Δt is chosen from the minimum of (4.1) and (4.2). For variable properties, as in our case, both (4.1) and (4.2) must be always examined for the minimum Δt. Note that the restriction (4.2) due to convection is of the order of $1/Ma$ larger than the one obtained if the acoustic waves had been left in the governing equations.

The predicted and corrected reduced pressure Π^+ and Π^{n+1} are obtained from the discretized equation (2.12) using a direct Poisson solver (Adams, Swarztrauber & Sweet 1981). This is the most time-consuming part of the program.

In problems which make use of the Boussinesq equations using primitive variables one must treat the divergence variable D defined by (2.11) carefully in solving the Poisson equation (2.12) in order to avoid a numerical instability (Harlow & Welch 1965; Hirt & Harlow 1967; Williams 1969). Note that in such a case D should be identically zero, as it is if one uses a stream-function treatment. However, because of round-off errors in solving (2.12) it is usually found that $D^n \neq 0$, and if this error is allowed to persist, a numerical instability manifests itself. In problems where the divergence of the velocity field should be zero this difficulty is resolved by using the round-off divergence at one timestep as a correction term in the right side of (2.12) and requiring that $D^{n+1} = 0$. In our case $D \neq 0$ except in the Boussinesq limit, and in addition, because of any errors in the time integration of (3.2), we cannot guarantee global mass conservation either (note that in the Boussinesq limit, (3.2) is identically zero). This dilemma is resolved with the following strategy.

In step 5 of the procedure, the predicted reduced pressure and momentum fluxes are corrected using (2.12) and (2.4) so that the variables correctly satisfy the momentum equations and the continuity equation (2.3) locally. However, since exact integration of (3.2) (which accounts for pressure variations produced by expansion and compression of the gas) cannot be obtained, $\bar{p}^+$ obtained in step 3 must be corrected to ensure global mass conservation also. This is done by starting from the perfect-gas law (3.1) with $Z = 1$ for a cell

$$\rho'_{i,j} = \frac{\bar{p}^+}{T^{n+1}_{i,j}}, \tag{4.3}$$

and computing the average density in the whole region

$$\rho' = \bar{p}^+ \sum_{i,j} \frac{1}{T^{n+1}_{i,j}}. \tag{4.4}$$

Now if we let $\rho^e_{i,j}$ be the unknown exact local density (note that we know the exact global density)

$$\rho^e_{i,j} = \rho'_{i,j} + \Delta\rho_{i,j} = \frac{\bar{p}^+ + \Delta\bar{p}}{T^{n+1}_{i,j}}, \tag{4.5}$$

and make use of (4.4), we obtain the following pressure correction necessary to give us global mass conservation

$$\Delta\bar{p} = \Delta\rho / \sum_{i,j} \frac{1}{T_{i,j}^{n+1}}, \tag{4.6}$$

where $\Delta\rho = \rho^c - \rho'$ is obtained by summing (4.5) over the complete region. Thus the overall pressure is finally corrected as

$$\bar{p}^{n+1} = \bar{p}^{+} + \Delta\bar{p}. \tag{4.7}$$

4.3. *The boundary conditions*

The fluid velocity is prescribed on the boundaries of the cavity. This is done in two different ways: at those points lying on a boundary we fix the corresponding velocity component to have the desired value, e.g. $u(\bullet) = 0$ at $x = 0, 1$; for those components for which the computational points do not fall on a boundary, we force two interior points and the point exterior to the boundary to have the desired value by adjusting the velocity at the outside points by quadratic extrapolation.

Temperature points do not lie on any boundary. Hence we force two interior points and the point exterior to the boundary to yield a constant temperature on the vertical walls and a zero flux on the horizontal walls by quadratic extrapolations.

In solving the discretized form of the Poisson equation (2.12), knowledge of the reduced pressure gradient normal to the walls is required. A simple and popular choice is to set this gradient to zero similar to boundary-layer flows. For physical reasons no boundary conditions for Π ought to be prescribed at the walls. A zero gradient normal to the walls, however, is not a bad approximation as long as the Rayleigh number is high, so that a boundary layer exists, and as long as this boundary layer is neither separated nor leaving the surface. Such is not the case in all wall regions of the cavity. A consistent and correct condition for the reduced pressure gradient is obtained by evaluating the momentum equations (2.4) at the walls.

5. Flow regions

The problem studied here (figure 1) is perhaps the most simple one possible involving convection heat transfer between two isothermal boundaries; in spite of this apparent simplicity, the physical nature of the resulting flow regions, even at steady state, can be an incredibly complex function of the three controlling independent dimensionless parameters A, Ra, and ϵ (for fixed Pr). Information gathered from an excess of two hundred detailed flow-field computations is used to construct the flow-regions map shown in figure 3, where A versus Ra is given for $1 \leqslant A \leqslant 10^2$ and $10^2 \leqslant Ra \leqslant 10^8$. The solid lines for the Boussinesq limit $\epsilon \ll 1$ and the dashed lines for $\epsilon = 0.6$ which bound some of the regions, denote lines of stability. The limits of the boundary-layer regimes are given by the dot–dash and the dotted lines, for $\epsilon \ll 1$ and $\epsilon = 0.6$, respectively. The shaded region represents the unsteady transition to turbulence for $\epsilon \ll 1$. Correlations defining boundaries of the regions shown in figure 3 are given below.

With the exception of the number of grids used as stated in table 2 regarding Richardson extrapolation, the bulk of computations were performed with a number of grids which varied with aspect ratio and Rayleigh number as given in table 1. Note that when a single number is given in the table, it implies that square grids were used, and when two numbers are given, the second number represents the number of grids used in the vertical direction. All computations were performed using uniform grids,

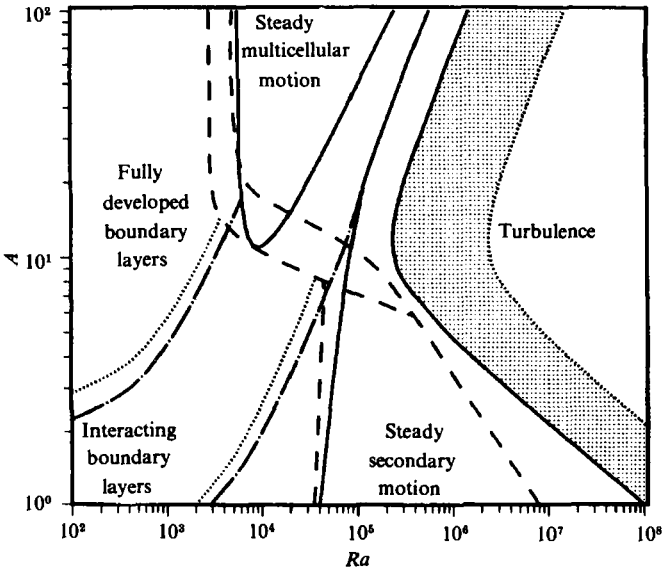

FIGURE 3. Flow regions dependence on A, Ra and ϵ; lines of stability: ——, $\epsilon \ll 1$, – – –, $\epsilon = 0.6$; boundary-layer regimes: —·—, $\epsilon \ll 1$, ·····, $\epsilon = 0.6$; dotted area denotes transition to turbulence.

		Ra					
		$[0, 10^3]$	$(10^3, 10^4]$	$(10^4, 10^5]$	$(10^5, 10^6]$	$(10^6, 10^7]$	$(10^7, 10^8]$
A	(1, 3]	21†	41	61	81	81‡	101‡
	(3, 5]	21 × 61†	41 × 61	61	81	81	—
	(5, 10]	21 × 81†	41 × 81	61 × 81	81	—	—
	(10, 100]	41 × 161	41 × 161	41 × 161‡	41 × 161‡	—	—

† To obtain accurate pressure and heat transfer results in the near-conduction region as many as 81 × 81 grids were found necessary for $1 \leqslant A \leqslant 3$, and 41 × 161 for $3 < A \leqslant 10$.

‡ To obtain enough resolution to determine the transition to oscillatory instabilities for $A = 1$ and 2, a non-uniform grid of 61 × 61 with a grid size ratio of $G = 0.03$ between the minimum and maximum in both directions was used for $Ra = 10^7$, 101 × 101 and $G = 0.3$ for $10^7 < Ra \leqslant 4 \times 10^7$, and 121 × 121 and $G = 0.2$ for $Ra > 4 \times 10^7$. For $A = 20$ and $10^4 < Ra \leqslant 10^6$, 61 × 161 grids with $G = 0.3$ was used.

TABLE 1. Grids used as a function of A and Ra.

except as noted in the table, where the non-uniform grid distribution described by Paolucci (1986) was used.

The most familiar flow region, often called the boundary-layer region, is characterized by independent (non-interacting) boundary layers on the hot and cold walls; here the boundary layers are separated by a nearly stagnant core which always displays an approximately linear vertical thermal stratification. The boundary-layer region exists primarily (although not exclusively) for low aspect ratios,

$$1 \leqslant A \leqslant \frac{12(1+4\epsilon)}{Ra^{0.25\epsilon}}, \tag{5.1}$$

and for Rayleigh numbers in the range

$$7 \times 10^3(A-0.6) < Ra < 10^4 A\left(1.5+\frac{10^4}{A^4}\right), \tag{5.2a}$$

for $\epsilon \ll 1$, and

$$4.5\times10^3(A-0.6) < Ra < \frac{8\times10^6A^{-1.7}+5\times10^3(\frac{1}{12}A)^6}{1+(\frac{1}{12}A)^6}, \tag{5.2b}$$

for $\epsilon = 0.6$. The upper limits in (5.2a, b) represent critical Rayleigh numbers, since above those limits the flow no longer reaches a steady state. When Ra is increased significantly above these critical values, the flow becomes increasingly unsteady and eventually becomes turbulent. The focus of this paper is primarily concerned with laminar convection. However, accurate detailed results for $A = 1$ and $Ra = 10^{10}$, computed from first principles with no empirical turbulence model, are presented in another paper (Paolucci 1986).

Below the lower limit of the independent boundary-layer region and for

$$400[A(1-\epsilon^3)-2] < Ra < 7\times10^3(1-\epsilon^2)(A-0.6), \tag{5.3}$$

and aspect ratios approximately in the range (5.1), the velocity boundary layers are interacting to an increasing degree as the value of Ra is decreased. Finally for

$$Ra < 400[A(1-\epsilon^3)-2], \tag{5.4}$$

fully developed merged boundary layers exist near the mid-height of the slot. At that point both velocity and temperature are within 3 % of universal profiles which are independent of the vertical coordinate. As the aspect ratio is increased further, the fully developed profiles exist in a region whose size is proportional to A, since the development regions near each end remain nearly fixed in size for given Ra and ϵ. The fully developed region is centred about $\frac{1}{2}A$ for small Ra, but for non-Boussinesq cases, when Ra is near the critical value of $5760(1+0.434\epsilon)^{-3}$ and $A > 11$, it may be centred significantly below $\frac{1}{2}A$, since near that limit the bottom development region is approximately half that found at the top of the slot.

For aspect ratios greater than 12–15, if the critical Rayleigh number of $5760(1+0.434\epsilon)^{-3}$ is exceeded, another type of instability can appear. This instability is characterized by standing waves and gives rise to multicellular flow inside the primary roll. Then combinations of large and small cells cover the entire slot and increase in strength with increasing Ra. The number and size of these cells depend on A, Ra and ϵ. We note that in the Boussinesq limit these cells are approximately the same size, their number depends only on aspect ratio, and their strength increases with increasing Ra (Lee & Korpela 1983). This multicellular motion is completely steady.

In the Boussinesq limit, as the Rayleigh number is further increased, a region of reverse transition from multicellular to unicellular flow exists. This region is bounded by the multicellular region described by

$$A > 4.2\times10^{-3}Ra^{1.31}(Ra-5760)^{-\frac{1}{2}}, \tag{5.5}$$

and by a thin boundary-layer region containing steady secondary motion described by

$$4\times10^4A^{\frac{1}{4}}(1+10^{-2}A^{\frac{5}{4}}) < Ra < 10^4A\left(1.5+\frac{10^4}{A^4}\right). \tag{5.6}$$

Above the upper limit of (5.6), unsteady motion exists. The region of secondary motion described by (5.6) is in fact also valid for low aspect ratios as shown in figure 3 and occupies most of the boundary-layer region defined by (5.2a). This is also true for $\epsilon = 0.6$, since for $A < 8$ the lower limit of (5.6) is then replaced by

$$Ra > 3.5\times10^4A^{\frac{1}{8}}. \tag{5.7}$$

The reverse transition region, whose boundaries merge as $A \to \infty$ for $\epsilon \ll 1$, does not exist for $\epsilon = 0.6$ since in this case the boundaries merge near the upper limit of (5.1) as shown in figure 3. In fact, in this case, the approximate expression (5.5) and the lower limit of (5.6) are now replaced by

$$Ra > 2880 + \left(\frac{40}{A}\right)^{6.67}, \tag{5.8}$$

so that strong multicellular motion is now present in this entire region. This large change for $A \gg 1$ and for $\epsilon = 0.6$ is accompanied by a greatly reduced critical Rayleigh number for unsteady motion as indicated by the upper limit of (5.2*b*). The steady multicellular region is now confined to a narrow region between (5.8) and the upper limit of (5.2*b*). The other large non-Boussinesq change occurs in the transition to unsteady flow at low aspect ratios. This effect is due to a change in the physical nature of the instability and will be discussed later.

6. Mass and heat constraints

For small-scale convection problems in the low-Mach-number limit, it has been shown (Paolucci 1982) that the pressure can be uncoupled into a spatially uniform static component $\bar{p}$ appearing in the equation of state (2.6) and energy equation (2.5), in addition to the small dynamic–hydrostatic component Π which must be retained in the momentum equations (2.4). Thus the spatial density variations are due entirely to thermal gradients rather than acoustic wave effects commonly encountered in high-speed flows.

The net vertical and horizontal mass fluxes can be written as

$$\omega = \int_0^1 \rho v \, \mathrm{d}x, \tag{6.1}$$

$$\chi = \int_0^A \rho u \, \mathrm{d}y, \tag{6.2}$$

at any y or x cross-section respectively. At steady state $\omega = \chi = 0$ so that (using (3.1) with $Z = 1$)

$$\int_0^1 \left(\frac{v}{T}\right) \mathrm{d}x = 0, \tag{6.3}$$

$$\int_0^A \left(\frac{u}{T}\right) \mathrm{d}y = 0. \tag{6.4}$$

since $\bar{p} \neq 0$. In the Boussinesq limit one can show that the solutions u, v and $T-1$ are antisymmetric about the centre point of the cavity, hence (6.1) and (6.2) with $\rho = 1$ yield no new information when applied to the cavity mid-sections. In contrast, in the non-Boussinesq case, the problem has no such symmetry, and thus (6.3) and (6.4) are non-trivial constraints on the solutions at the mid-sections, as well as at other sections.

The constant-mass constraint

$$\int_0^A \int_0^1 \rho \, \mathrm{d}x \, \mathrm{d}y = A, \tag{6.5}$$

can be used to obtain an expression for $\bar{p}$

$$\bar{p} = A \Big/ \int_0^A \int_0^1 T^{-1} \, \mathrm{d}x \, \mathrm{d}y, \tag{6.6}$$

which is valid at all times. Even in the simple limits of constant properties, zero Rayleigh number and steady-state, where T is linear in x and ϵ, $\bar{p}$ can be unity only in the Boussinesq limit $\epsilon \to 0$, and $\bar{p} < 1$ for any $\epsilon \neq 0$, since

$$\bar{p} = 2\epsilon / \ln\left(\frac{1+\epsilon}{1-\epsilon}\right) \approx 1 - \tfrac{1}{3}\epsilon^2 - \tfrac{4}{45}\epsilon^4 - \ldots \tag{6.7}$$

in that case. The pressure corresponding to Sutherland-law conductivity in the conduction limit is more complicated (Chenoweth & Paolucci 1985). In general (for fixed Prandtl number)

$$T = T(t, x, y, \epsilon, Ra, A), \tag{6.8}$$

and the resulting pressure level depends on time as well as the three parameters ϵ, Ra and A

$$\bar{p} = \bar{p}(t, \epsilon, Ra, A), \tag{6.9}$$

and a rather complex behaviour results from (6.6).

The net vertical heat flux can be expressed for any y cross-section as

$$q = \int_0^1 \left[\rho v T - k \frac{\partial T}{\partial y}\right] \mathrm{d}x, \tag{6.10}$$

which becomes

$$q = \bar{p} \int_0^1 v \, \mathrm{d}x, \tag{6.11}$$

in the fully developed region where $\partial T/\partial y \approx 0$. Then, using solutions for $\bar{p}$ and v obtained by Chenoweth & Paolucci (1985) for steady state we obtain

$$q \approx \epsilon \frac{Ra}{360}, \tag{6.12}$$

which is positive and proportional to both ϵ and Ra (but independent of A). Note from (6.10) that the same result is obtained in the Boussinesq limit (Batchelor 1954) by setting $\rho = 1$. Since the horizontal heat flux in the fully developed region is $Q_c = k \partial T/\partial x \approx -2\epsilon$ (Chenoweth & Paolucci 1985) then

$$\frac{q}{Q_c} \approx -\frac{Ra}{720}, \tag{6.13}$$

and the magnitude of q is comparable to that of Q_c when Ra is approximately 720. Here, and in the following sections, the subscripts c, n and b denote conduction, near-conduction and boundary-layer regions, respectively. Although the total heat flow at the hot wall is equal to that at the cold wall at steady state, the distributions of the local heat flux on the hot and cold walls in the developing end regions are no longer antisymmetric for non-Boussinesq cases, and they become more antisymmetric for increasing ϵ or Ra. Notice that (6.13) shows that for low aspect ratios, but greater than 2 (see (5.4)), the conduction solution can only be valid for Ra values substantially less than 720 since the ratio between the vertical and horizontal heat flows must be negligible in that limit, i.e. $|2q/AQ_c| \ll 1$. We note that (6.13) is independent of ϵ, and (6.12) and (6.13) are the same as values obtained from Boussinesq equations, hence they are independent of property variations.

In the independent boundary-layer region $\partial T/\partial y \neq 0$, but it is approximately constant and independent of Ra. Specifically

$$\left(\frac{\partial T}{\partial y}\right)_{x=\frac{1}{2}} \approx \frac{2\epsilon}{A}, \tag{6.14}$$

while the vertical velocity increases strongly with the Rayleigh number (Gill 1966). Thus at large Ra it can be expected that the term involving $\partial T/\partial y$ in (6.10) is dominated by the term involving the vertical velocity. From the same numerous computations reported in detail in §8, we find that

$$q \approx 0.14\epsilon A Ra^{0.29} \tag{6.15}$$

approximately describes the behaviour of the vertical heat flux in the independent boundary-layer region (5.1)–(5.2a, b) within $\pm 13\%$. Actually the aspect-ratio dependence of q is more complicated than the simple linear one shown above. Within $\pm 6\%$ error

$$q \approx 0.46 A \bar{Q}_b. \tag{6.16}$$

where $A\bar{Q} = \int_0^A Q\,dy$ is the total horizontal heat flow, and is given by (8.10). Also about 63 % (59–67 %) of the total heat flowing in from the bottom half of the slot (virtually all of which is convected into the top half) is transferred out from the top half of the slot before the remainder returns to the bottom half where it is transferred out. We find that, essentially independent of Ra, ϵ and A (within the accuracy stated), 73 % of the total heat comes into the slot from the bottom half of the hot wall and the same amount exits through the top half of the cold wall, consistent with the above picture. Here the nearly linear aspect-ratio dependence and $Ra^{0.29}$ dependence in (6.15) is to be contrasted to the linear Ra dependence of (6.12) which is independent of A in the fully developed region.

7. Code validation

Chenoweth & Paolucci (1985) give the exact non-Boussinesq conduction solution ($Ra \to 0$) for the temperature profiles, heat flux Q_c, and the pressure level $\bar{p}_c$ with Sutherland-law conductivity. Since Q_c and $\bar{p}_c$ are used here to normalize our results, we reproduce those equations for convenience:

$$Q_c = 2(1+S_k)\,S_k^{\frac{3}{2}}(f_1 - f_0), \tag{7.1}$$

$$\bar{p}_c = \frac{S_k(f_1 - f_0)}{(F_1 - F_0)}, \tag{7.2}$$

where the subscripts 0 and 1 denote that the functions are to be evaluated at $x = 0$ and 1 respectively, and

$$f = \frac{1}{3}\left(\frac{T}{S_k}\right)^{\frac{3}{2}} - F,$$

$$F = \left(\frac{T}{S_k}\right)^{\frac{1}{2}} - \tan^{-1}\left(\frac{T}{S_k}\right)^{\frac{1}{2}}.$$

For $\epsilon = 0.6$, Q_c is only 2 % below the constant conductivity value of -2ϵ, whereas $\bar{p}_c$ is approximately 0.9904 or 14.4 % above the constant property result of 0.8656 obtained from (6.7). In the Boussinesq limit, Batchelor (1954) shows that $(\bar{Q}_n/Q_c - 1)$ is proportional to Ra^2 for low Ra values (e.g. $Ra < 500$) and it is inversely proportional to A for large A. In addition, Chenoweth & Paolucci (1985) derive exact non-Boussinesq solutions for the fully developed velocity profiles with Sutherland-law properties which are valid for a large parameter range. These exact solutions are generalizations of the well-known cubic solution (Batchelor 1954) valid in the Boussinesq limit. There are also well-established Boussinesq results (De Vahl Davis

1983) in the boundary-layer region and developing boundary-layer region for velocity, temperature and Nusselt number. The wide variety of results just mentioned are used to validate the computer program prior to the presentation of other non-Boussinesq results.

7.1. *Conduction and near-conduction regions*

For constant conductivity, the conduction solution is easily reproduced numerically for all ϵ values due to the linear temperature profiles. However, for Sutherland-law conductivity, it is much more difficult to reproduce for large ϵ since the temperature profiles become increasingly nonlinear near the cold wall, where an infinite gradient develops as ϵ approaches unity. The pressure level is a good measure of the numerical resolution required to properly describe that region. Figure 4 presents $\bar{p}$ versus the number of grid points for $\epsilon = 0.6$, $A = 1$, and several values of Ra. It is clear that in order to obtain four significant figures accuracy for $\bar{p}$, more than 80 grid points are needed in this highly non-Boussinesq case. Furthermore, it can be seen that $Ra < 10^2$ is required in order to recover the conduction solution to the same level of accuracy. The results on figure 4 also show that the order of truncation error is near 2.

We investigate the near-conduction region $Ra \leqslant 5 \times 10^2$ for $A \geqslant 1$ and $0 \leqslant \epsilon \leqslant 0.6$ to better understand the detailed behaviour with each of the parameters. It was found that for large ϵ, both the heat flux and the pressure depart from conduction values with the Ra^2 dependence; also for $A \gg 1$ both $(\bar{Q}_n - Q_c)$ and $(\bar{p}_n - \bar{p}_c)$ have inverse A dependence although their dependence on A is complicated as $A \to 1$ by the existence of a maximum for Nu_n and a minimum for $\bar{p}_n$ near $A = 1.65$. This behaviour is shown in figure 5, which gives $Nu_n - 1$ versus A for $Ra = 10^2$ and two values of ϵ. The correlating equations

$$Nu_n - 1 = 0.584(1-\epsilon^5)\left(\frac{Ra}{10^3}\right)^2\left[\frac{A^4}{(3+A^5)}\right], \tag{7.3}$$

$$\bar{p}_n/\bar{p}_c - 1 = -(\tfrac{1}{2}\epsilon^3)\left(\frac{Ra}{10^3}\right)^2\left[\frac{A^4}{(3+A^5)}\right], \tag{7.4}$$

accurately describe the behaviour just outlined. A major difference in $Nu_n = \bar{Q}_n/Q_c$ and $\bar{p}_n/\bar{p}_c$ is the ϵ dependence. The weak ϵ^5 dependence of Nu_n can generally be neglected. However, the entire departure of $\bar{p}_n$ from $\bar{p}_c$ is due to non-Boussinesq effects described by the ϵ^3 dependence as shown in (7.4). For $Ra > 5 \times 10^2$ the Ra and A dependence of $Nu - 1$ and $\bar{p}/\bar{p}_c - 1$ are no longer the same, and both are significantly different from (7.3) and (7.4), as will be shown in the following sections.

7.2. *Fully developed region*

The conduction temperature profiles are actually valid for a much larger parameter region than that included in the conduction ($Ra < 10^2$) or near-conduction ($Ra \leqslant 5 \times 10^2$) regions:

$$Ra < Ra_c = 5760(1+0.434\epsilon)^{-3}, \tag{7.5}$$

$$A > A_d = \frac{(2+Ra/400)}{(1-\epsilon^3)}. \tag{7.6}$$

Chenoweth & Paolucci (1985) derive the corresponding exact velocity profiles valid in this large parameter region. The solutions are valid only in the mid-region of the

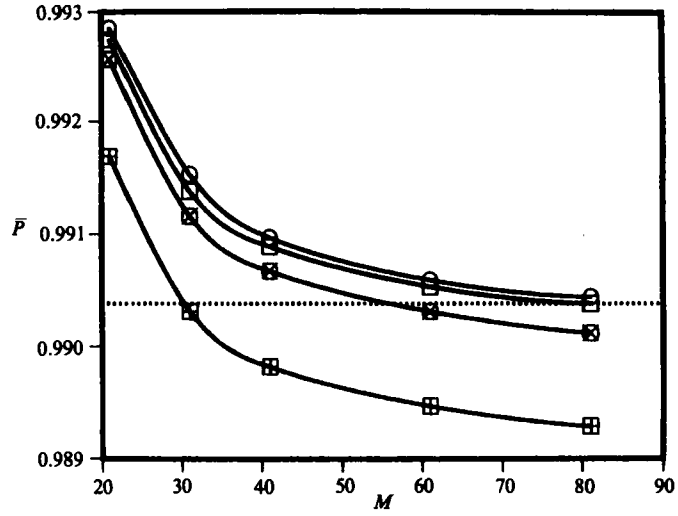

FIGURE 4. Pressure versus number of grid points M in each coordinate direction for $A = 1$, $\epsilon = 0.6$ and various Rayleigh numbers: ·····, $Ra = 0$(*exact*); ⊙, $Ra = 10$; □, $Ra = 50$; ⊗, $Ra = 100$; ⊞, $Ra = 200$.

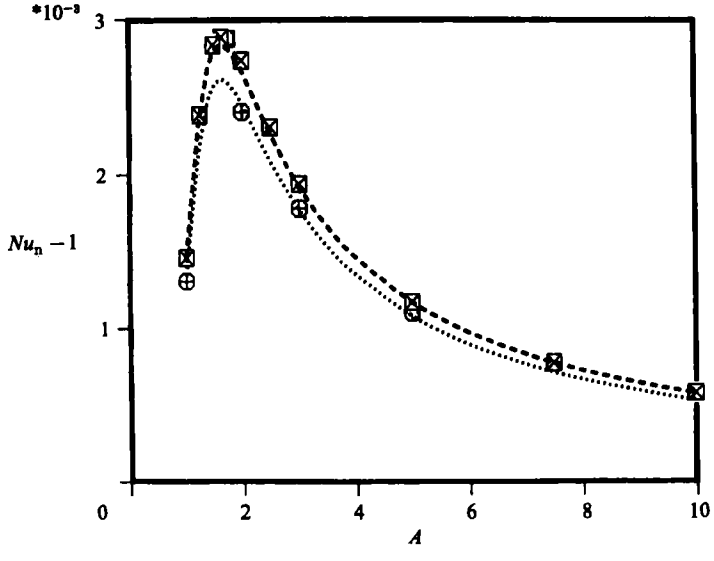

FIGURE 5. Near conduction $Nu_n - 1$ versus A for $Ra = 100$; Numerical: ⊠, $\epsilon = 0.005$, ⊕, $\epsilon = 0.6$. Equation (7.3): - - - - -, $\epsilon = 0.005$, ·····, $\epsilon = 0.6$.

slot a few slot widths away from the ends. The condition (7.6) is required in order that the fully developed velocity profiles occur; the extent of the region where these profiles are fully developed and free of end effects is roughly given by $(A - A_d)$. The exact solution not only displays most of the physical features which characterize non-Boussinesq problems, but it is also valuable to validate large computer programs in the highly non-Boussinesq regime. Such a comparison is given in figure 6 for the temperature and velocity profiles. Here only selected coordinate points for each case are shown, to aid clarity of presentation. The results are for $\epsilon = 0.6$ with the aspect

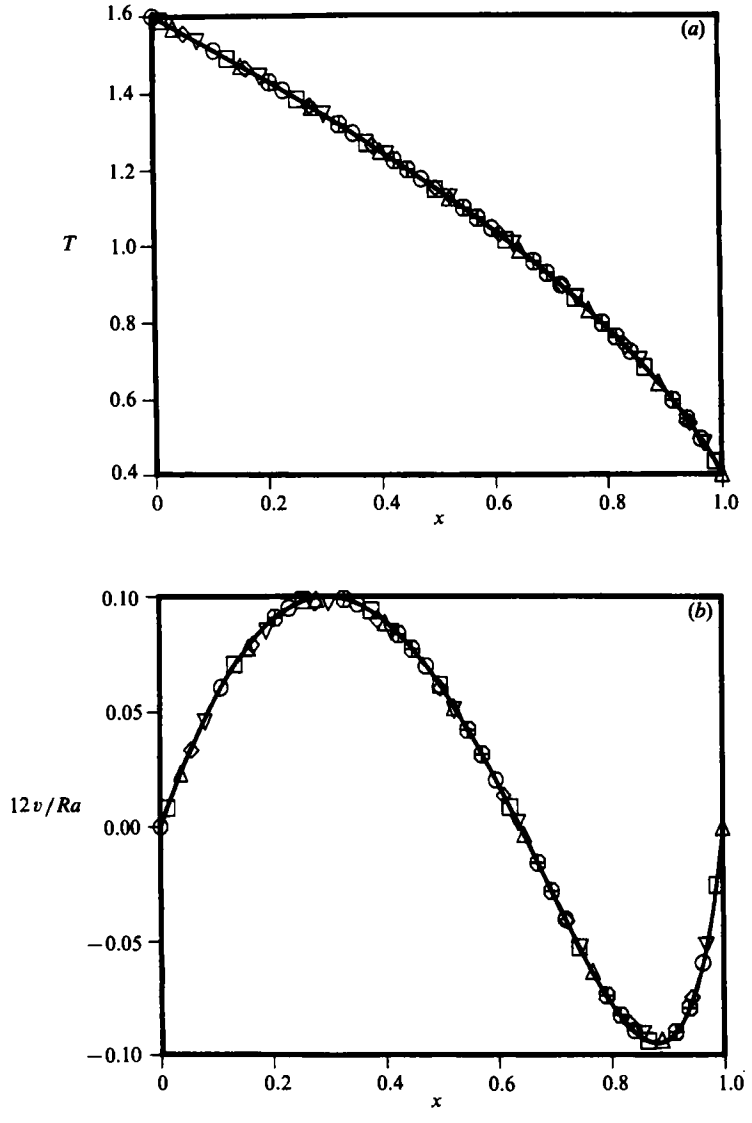

FIGURE 6. Exact-solution profiles compared to numerical results for $\epsilon = 0.6$: (*a*) Temperature; (*b*) Velocity. $A = 3$: $\oplus$, $Ra = 10^{-2}$; $\odot$, $Ra = 1$; $\square$, $Ra = 10^2$. $A = 5$: $\diamond$, $Ra = 5 \times 10^2$. $A = 20$: ∇, $Ra = 3 \times 10^3$. $A = 40$: $\triangle$, $Ra = 5 \times 10^2$.

ratio varied from 3 to 40 and the Rayleigh number varied from 10^{-2} to 3×10^3 within the region bounded by (7.5) and (7.6). The results illustrate that the mid-slot profiles for temperatures are indeed conduction profiles and are independent of both A and Ra. The increased nonlinearity of T near the cold wall, where a steeper gradient exists, is also evident in figure 6(*a*). Since the velocity in figure 6(*b*) is scaled by Ra^{-1}, it is clear that v depends linearly on Ra and is independent of A in this region. The much thinner velocity layer on the cold wall compared to the hot wall is also very noticeable on the figure. The high-Ra results are approximately 3% below the exact solution, since the exact solution does not account for multi-dimensional end effects, thus causing $\bar{p} < \bar{p}_c$. The use of (7.4) for $Ra \leqslant 500$, or some other result valid for $Ra < Ra_c$

instead of $\bar{p} = \bar{p}_c$, to extend the range of validity of the exact solution can correct for such effects if higher accuracy is desired for the validation. In fact for $A > Ra^{\frac{1}{4}}$, and with little loss of accuracy, we have found that (7.3) and (7.4), describing the Nusselt number and pressure variations in the near-conduction region, can be extended up to Ra_c given by (7.5), where standing waves transition occurs, by the following

$$(Nu-1)\,A = \frac{0.584(Ra/10^3)^2}{1+0.5(Ra/10^3)}, \tag{7.7}$$

$$(1-\bar{p}/\bar{p}_c)\,A = \frac{0.5\epsilon^3(Ra/10^3)^2}{1+2.4\epsilon^{\frac{3}{2}}(Ra/10^3)^{\frac{3}{2}}}. \tag{7.8}$$

7.3. *Boussinesq boundary-layer results*

In this section steady-state Boussinesq results for $Ra = 10^3 - 10^6$ and $A = 1$ are compared to the numerical solutions of De Vahl Davis (1983). His solutions to the above problem, obtained via Richardson extrapolations, served as a 'bench mark' for a comparison exercise (De Vahl Davis & Jones 1983). Table 2 gives our results obtained with square grids ($\Delta x = 1/M$, $\Delta y = 1/N$ and $M = N$) varying in number from 11 to 101. In the table we present the average wall Nusselt number Nu, the maximum horizontal and vertical velocities u_{max} and v_{max} at the mid-width and mid-height, and their respective y and x locations. The Nusselt number is obtained by averaging the heat flux over the hot and cold wall. At steady state the results from the hot and cold wall agreed within the accuracy reported in the table and hence no labelling is necessary. Since for $\epsilon \ll 1$ the problem displays full antisymmetry with respect to the centre of the cavity, only the positive velocity values are given. The values under 'exact' are obtained by Richardson extrapolation using the three results given in the table, and as such are sixth-order accurate.

The numbers is parentheses ( ) following the numerical results represent the magnitude of the percentage error between those results and the 'exact' values. Since the table values were rounded to four significant figures after calculating the errors, the errors in the table do not correspond exactly to the rounded numbers. Note that the errors in the table reflect the spatial second-order accuracy of the numerical scheme. The numbers in brackets [ ] following the 'exact' values give the magnitude of the percentage difference between these results and those of De Vahl Davis (1983). We note that De Vahl Davis used results of two differing grid sizes to obtain his extrapolated solutions, and hence his 'exact' solutions are fourth-order accurate, since his scheme was also spatially second order. We also note that we compare our average wall Nusselt number with his Nusselt number averaged throughout the cavity, since his average values at the hot wall and at $x = 0.5$ were not equal. The magnitude of the percentage difference between our 'exact' results and those of De Vahl Davis is approximately within his estimated errors of 0.1, 0.2, 0.3 and 1.0% at $Ra = 10^3$, 10^4, 10^5 and 10^6 respectively.

The importance of the above comparison is further appreciated if note is made that De Vahl Davis (1983) obtained his numerical results via a false transient integration of the Boussinesq equations using a vorticity-stream function formulation, while ours are obtained via a time-accurate integration of non-Boussinesq equations for $\epsilon = 0.005$ using a primitive variables formulation.

For completeness, in table 3 we present similar results for $A = 1$, and for higher Rayleigh numbers within the steady boundary-layer region. It is noted that Le Quere & Alziary de Roquefort (1985), using a spectral method with 65×65 modes, obtained

			$Ra = 10^3$					
M	11		21		41		'Exact'	
Nu	1.121	(0.26)	1.118	(0.05)	1.118	(0.01)	1.118	[0.01]
u_{max}	3.565	(2.29)	3.620	(0.78)	3.641	(0.22)	3.649	[0.00]
y	0.8142	(0.13)	0.8133	(0.01)	0.8132	(0.00)	0.8132	[0.02]
v_{max}	3.598	(2.64)	3.666	(0.80)	3.687	(0.22)	3.695	[0.05]
x	0.1766	(1.17)	0.1783	(0.22)	0.1786	(0.05)	0.1787	[0.39]
			$Ra = 10^4$					
M	21		41		61		'Exact'	
Nu	2.264	(0.91)	2.249	(0.24)	2.246	(0.11)	2.244	[0.02]
u_{max}	15.89	(1.84)	16.10	(0.53)	16.15	(0.24)	16.19	[0.05]
y	0.8229	(0.02)	0.8231	(0.00)	0.8231	(0.00)	0.8231	[0.01]
v_{max}	19.29	(1.73)	19.53	(0.50)	19.58	(0.23)	19.62	[0.04]
x	0.1175	(1.40)	0.1186	(0.48)	0.1189	(0.23)	0.1192	[0.14]
			$Ra = 10^5$					
M	41		61		81		'Exact'	
Nu	4.567	(1.05)	4.540	(0.45)	4.531	(0.25)	4.520	[0.02]
u_{max}	34.23	(1.56)	34.51	(0.76)	34.62	(0.44)	34.77	[0.11]
y	0.8551	(0.05)	0.8549	(0.03)	0.8548	(0.02)	0.8546	[0.04]
v_{max}	67.71	(1.34)	68.18	(0.66)	68.37	(0.38)	68.63	[0.06]
x	0.0653	(0.91)	0.0657	(0.30)	0.0658	(0.15)	0.0659	[0.16]
			$Ra = 10^6$					
M	61		81		101		'Exact'	
Nu	8.988	(1.88)	8.907	(0.96)	8.874	(0.59)	8.822	[0.25]
u_{max}	63.76	(1.76)	64.18	(1.12)	64.42	(0.76)	64.91	[0.43]
y	0.8547	(0.57)	0.8528	(0.35)	0.8518	(0.23)	0.8498	[0.02]
v_{max}	216.1	(2.13)	217.8	(1.36)	218.8	(0.92)	220.8	[0.65]
x	0.0372	(2.44)	0.0374	(1.92)	0.0376	(1.39)	0.0381	[0.61]

TABLE 2. Convergence of the solutions for $Ra = 10^3$–10^6 in the Boussinesq limit.

Ra	10^7	4×10^7	8×10^7
Nu	16.82	23.85	28.57
u_{max}	146	252	305
y	0.881	0.934	0.937
v_{max}	699	1390	1970
x	0.0213	0.0153	0.0130

TABLE 3. Boussinesq results for $Ra = 10^7 - 8 \times 10^7$.

$Nu = 16.52$, $u_{max} = 148.8$, $y = 0.879$, $v_{max} = 699.3$ and $x = 0.0213$ for $Ra = 10^7$, and $Nu = 23.82$ for $Ra = 4 \times 10^7$ (they did not report maximum velocity data at the higher Rayleigh number). Again, our results are in excellent agreement with the above values.

8. Boundary-layer region

In this section we examine the parameter space region included by (5.1), the upper limit of (5.2a) or (5.2b), and the lower limit of (5.3). This region includes most, but not all, of the independent boundary-layer and the developing merged boundary-layer regions.

8.1. *Velocity and temperature fields*

Some steady-state results in the form of velocity and thermal fields are given first to show the effect of ϵ throughout the above range of A and Ra. We note that in displaying the velocity fields we only show vectors on an interpolated matrix of 25×25 evenly spaced grids in figures 7–10, and on a 51×51 grid in figure 11, even though the number of computed values may be much greater and the computed grids non-uniform; also the vector-length normalization is different in each figure. In displaying the temperature fields in the figures, we always display 21 isoline levels using equal increments regardless of the magnitude of ϵ. We finally note that in figures 9(*c*)–(*d*) and 10 we normalize the vertical scale to be the same regardless of aspect ratio, so as to show more detail in the horizontal direction for the lower aspect ratios.

Figures 7(*a*)–(*d*) show velocity and temperature isolines for $A = 1$, $Ra = 10^5$ and $\epsilon = 0.005, 0.2, 0.4, 0.6$ within the region of secondary motion (see figure 3). The most apparent effect is the increasing asymmetry, which increases linearly with ϵ. There is a very pronounced shift of the centre of the primary vortex, which gives rise to the roll motion, both towards the cold wall and downwards towards the lower end of the cavity. The reason for this shift arises primarily from the source of vorticity due to buoyancy, i.e. $(Ra\,Pr/2\epsilon)\,(\bar{p}/T^2)\,\partial T/\partial x$. The temperature gradient is highest on the vertical walls, and the gas is colder near the right and bottom walls than near the left and top walls. The effect of this primary source of vorticity is modified somewhat from the presence of a secondary source not present in the Boussinesq case, i.e. $-\nabla\rho \times \nabla(\frac{1}{2}v^2)$. Note that this secondary source, in contrast to the primary one, is weakest near the vertical walls, where the gradients of density and velocity are nearly parallel.

Figures 8(*a*)–(*d*) show similar results for $A = 1$, $\epsilon = 0.6$ and $Ra = 10^3, 10^4, 10^5, 10^6$. Here the boundary-layer thickness decreases on both hot and cold walls with increasing Ra in proportion to $Ra^{-\frac{1}{4}}$. This is of course accompanied by an increase in velocity as the boundary layers become thinner. The well-known (Elder 1965; Gill 1966; Roux *et al.* 1978; Schinkel, Linthorst & Hoogendoorn 1980) scaling for maximum velocity $\pm 0.22(RaA)^{\frac{1}{2}}$ at the mid-height $y = \frac{1}{2}A$, valid in the $\epsilon \ll 1$ limit in the independent boundary-layer region (5.1) and (5.2*a*), is easily modified to include the ϵ dependence. The relatively weak linear ϵ dependence can be described by

$$v_+ = 0.22(RaA)^{\frac{1}{2}}\,(1 - 10^{-3}\epsilon Ra^{0.2}A^{-\frac{1}{2}}), \tag{8.1}$$

$$v_- = -0.22\,(RaA)^{\frac{1}{2}}\,(1 - 10^{-2}\epsilon Ra^{0.2}A^{-\frac{1}{2}}), \tag{8.2}$$

showing a small reduction in velocity with increasing ϵ in both cases, but a substantially larger reduction near the cold wall than is observed near the hot wall. The accompanying boundary-layer thinning can be observed from the location of the maximum velocity points

$$x_+ = 1.2\left(\frac{A}{Ra}\right)^{\frac{1}{4}}(1 + 0.82\epsilon), \tag{8.3}$$

$$x_- = 1 - 1.2\left(\frac{A}{Ra}\right)^{\frac{1}{4}}(1 - 0.75\epsilon A^{-\frac{1}{4}}), \tag{8.4}$$

which also show linear ϵ dependence, but here it is a very significant effect. For given A and Ra the hot-wall layer thickens by a larger amount than the cold-wall layer thins out. The cold-wall layer has an additional A dependence which causes further reduction in the shift towards the wall for $A > 1$.

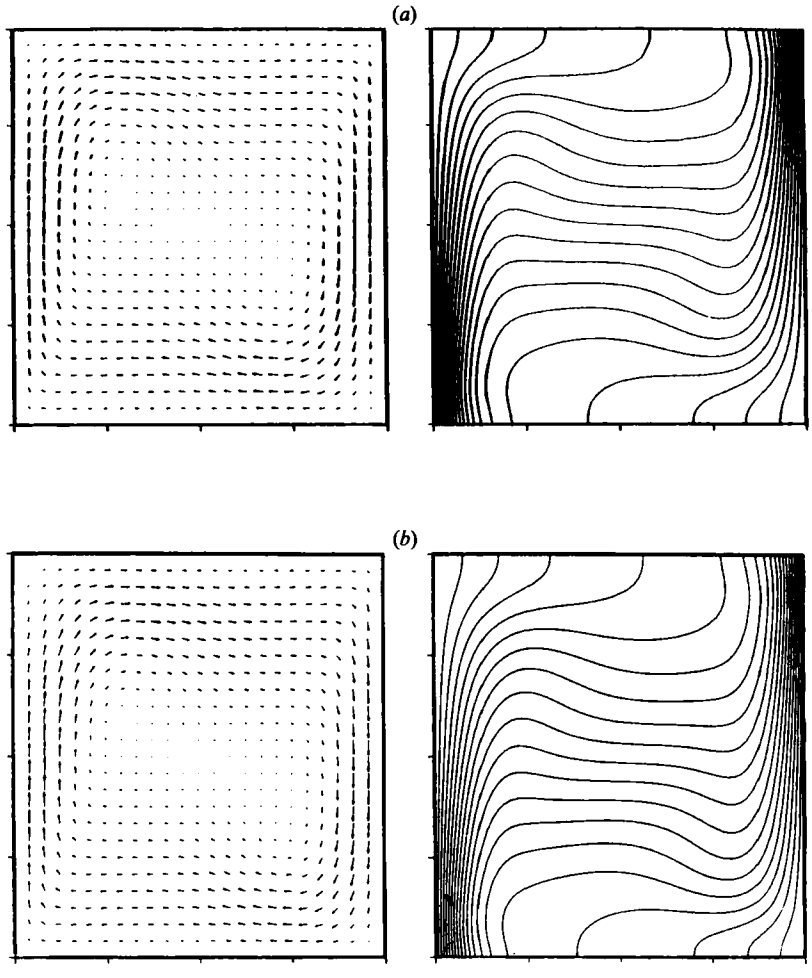

FIGURE 7(*a*, *b*). For caption see facing page.

The results for the independent boundary-layer region given by (8.1)–(8.4) are substantially different from those found in the fully developed region defined by (7.5) and (7.6), where everything is independent of A, although the linear dependence on ϵ is similar. In this region the velocity scales linearly with Ra for all ϵ (see Chenoweth & Paolucci 1985):

$$v_+ = \frac{(1+6\times10^{-2}\epsilon)\,Ra}{72\sqrt{3}}, \tag{8.5}$$

$$v_- = \frac{-(1-3\times10^{-2}\epsilon)\,Ra}{72\sqrt{3}}. \tag{8.6}$$

However, compared with (8.1)–(8.2), the positive maximum in (8.5) shows a linear increase with ϵ while the negative maximum in (8.6) shows a smaller linear decrease with ϵ. Also the linear shift of these maxima locations toward the cold wall with ϵ is independent of Ra and given by

$$x_+ = 0.211(1+0.706\epsilon), \tag{8.7}$$

$$x_- = 1.0-0.211(1-0.739\epsilon), \tag{8.8}$$

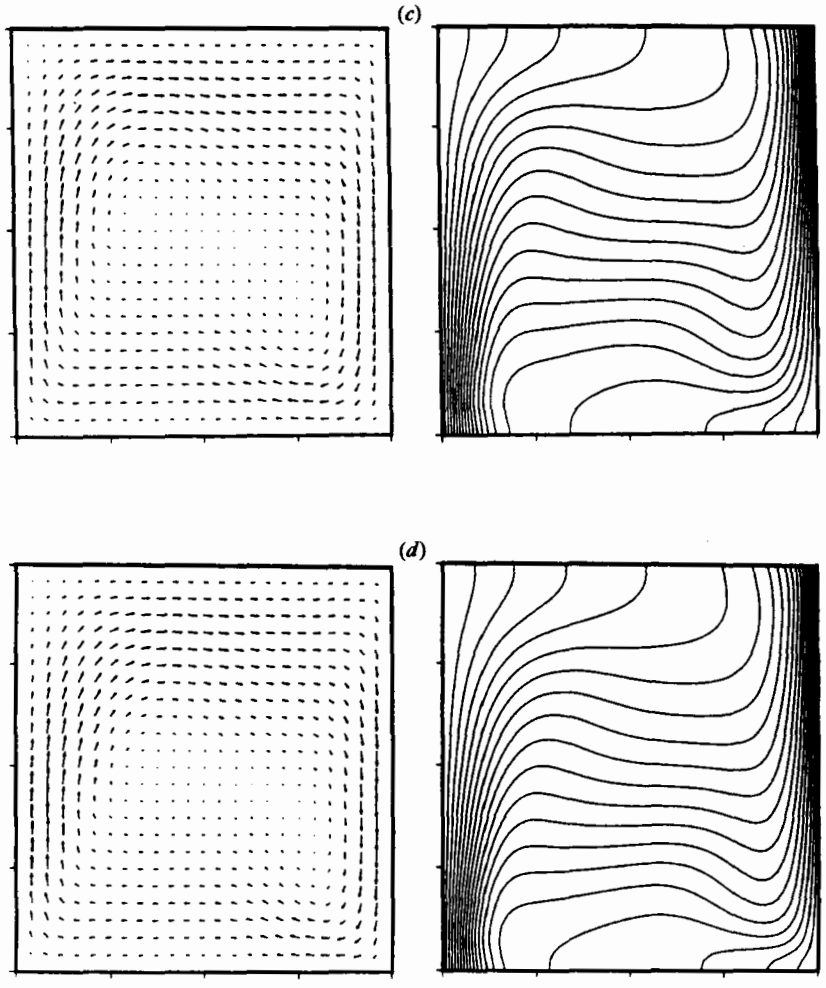

FIGURE 7. Velocity and isotherm fields for $A = 1$ and $Ra = 10^5$, with ϵ as the parameter; (*a*) $\epsilon = 0.005$, (*b*) $\epsilon = 0.2$, (*c*) $\epsilon = 0.4$, (*d*) $\epsilon = 0.6$.

so that, compared with (8.3)–(8.4), the effect of ϵ is slightly less here, and the negative maximum shifts more than the positive maximum.

As a final observation, from figures 8(*b*)–(*c*) we see the appearance in the core of the cavity of two weak vortices giving rise to secondary motion inside the primary roll. Their appearance is a direct consequence of changes in sign of the primary source of vorticity. This is due to the occurrence of inversions in the horizontal temperature gradient near the edges of the boundary layers (Mallinson & De Vahl Davis 1977). The presence of a secondary source of vorticity, due entirely to non-Boussinesq effects, modifies the above picture somewhat. In addition, viscous diffusion retards the development of these secondary rolls to a higher Rayleigh number.

Figures 9(*a*)–(*d*) give velocity and temperature isolines for $\epsilon = 0.6$, $Ra = 10^5$ and $A = 1, 2, 4$ and 6. For $\epsilon = 0.005$ we observe secondary rolls for Ra in the range given by (5.6) and (5.2*a*), while for $\epsilon = 0.6$ they are observed in the range given by (5.7) and (5.2*b*). Note that the multicellular region and the region of secondary flow, which were distinct in the Boussinesq limit, merge near the lower boundary of the region

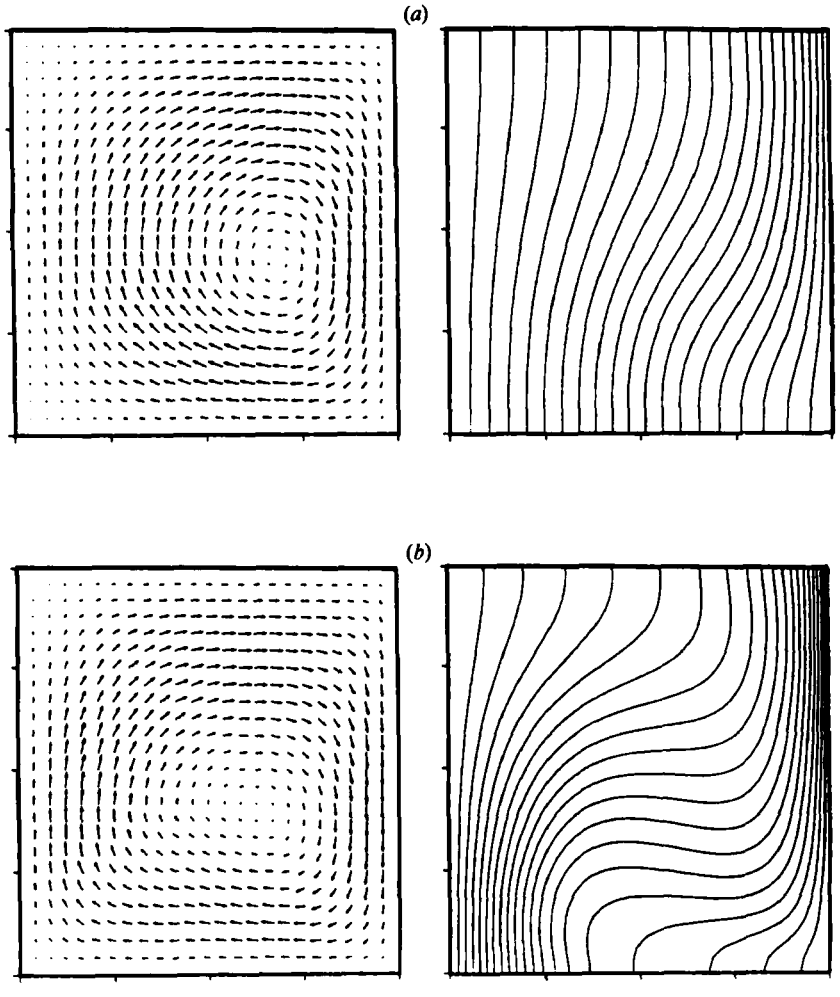

FIGURE 8(a, b). For caption see facing page.

defined by (5.8). For $Ra = 10^5$, between $A = 7$ and 8, there is a shift from weak secondary motion to strong cellular motion, as can be seen in figure 10. Evidently, as can be seen from figure 3, the condition of $Ra/A > 2.5 \times 10^4$ put forth by Schinkel *et al.* (1980) for $A > 2$ and for perfectly conducting end walls as necessary for the appearance of secondary rolls is modified. The $A = 7$ case is near the top of the independent boundary-layer region for $\epsilon = 0.6$ (see figure 3). For substantially larger Ra we enter the travelling-wave region and for substantially smaller Ra we enter the interacting boundary-layer region.

It was mentioned in the discussion of flow regions described by figure 3 that a large non-Boussinesq effect involves the replacement of (5.5) by (5.8) for $\epsilon = 0.6$. This limit describes the lower limit of multicellular motion and it shows that such motion occurs at much lower aspect ratios than in the Boussinesq case. Below the region defined by (5.8) and for Ra satisfying (5.7), stable steady-state motion with a single primary roll exists, provided the Ra value is not so large that the flow becomes unsteady. During the transition to steady state, unstable motion is observed in the bottom-end region for aspect ratios as small as 3 for $Ra = 10^5$ and $\epsilon = 0.6$, even though the flow

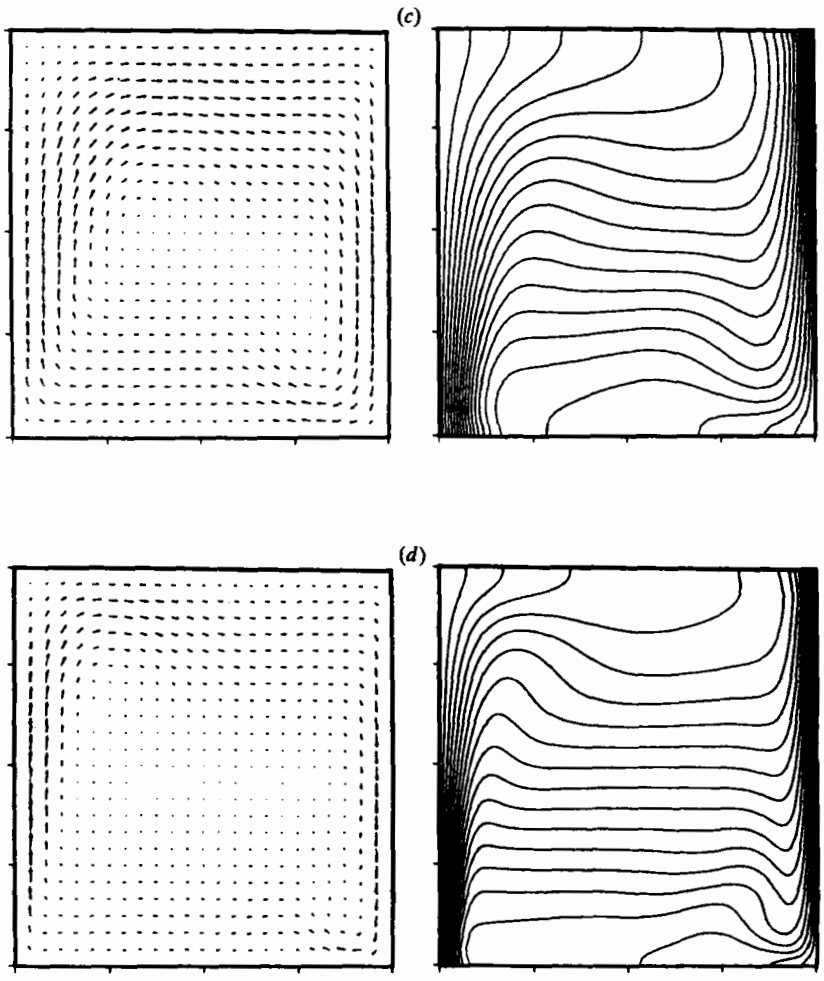

FIGURE 8. Velocity and isotherm fields for $A = 1$ and $\epsilon = 0.6$, with Ra as the parameter; (*a*) $Ra = 10^3$, (*b*) $Ra = 10^4$, (*c*) $Ra = 10^5$, (*d*) $Ra = 10^6$.

returned to a stable steady state with a single primary roll (Chenoweth & Paolucci 1986). This phenomenon is observed for aspect ratios as large as 7, whose steady-state results are displayed in figure 10(*a*). However, for $A = 8$ shown in figure 10(*b*) an intense vortex is centred near $y = 2.5$. Similarly figure 10(*c*) for $A = 10$ shows two intense vortices, one centred at $y = 2.5$ and another at $y = 5.5$. For comparison, figure 10(*d*) shows the result for $\epsilon = 0.005$, $Ra = 10^5$ and $A = 10$. Thus in the Boussinesq limit only a single primary roll exists for quite large aspect ratios. Even though the average heat transfer for figures 10(*c*) and (*d*) is approximately the same, the local heat transfer is much higher in the vicinity of the vortices when $\epsilon = 0.6$.

The other large non-Boussinesq effect occurs at low aspect ratios in the transition to unsteady flow. If one considers the internal Froude number (see Paolucci 1986) of the warm fluid turning at the top corner, if the flow is subcritical it spreads out smoothly over the heavier fluid as the intrusion approaches the cold wall. If the flow is supercritical a 'hydraulic' jump will occur. The energy loss associated with the jump is dissipated in a stationary wavetrain downstream of it. This is illustrated in figure

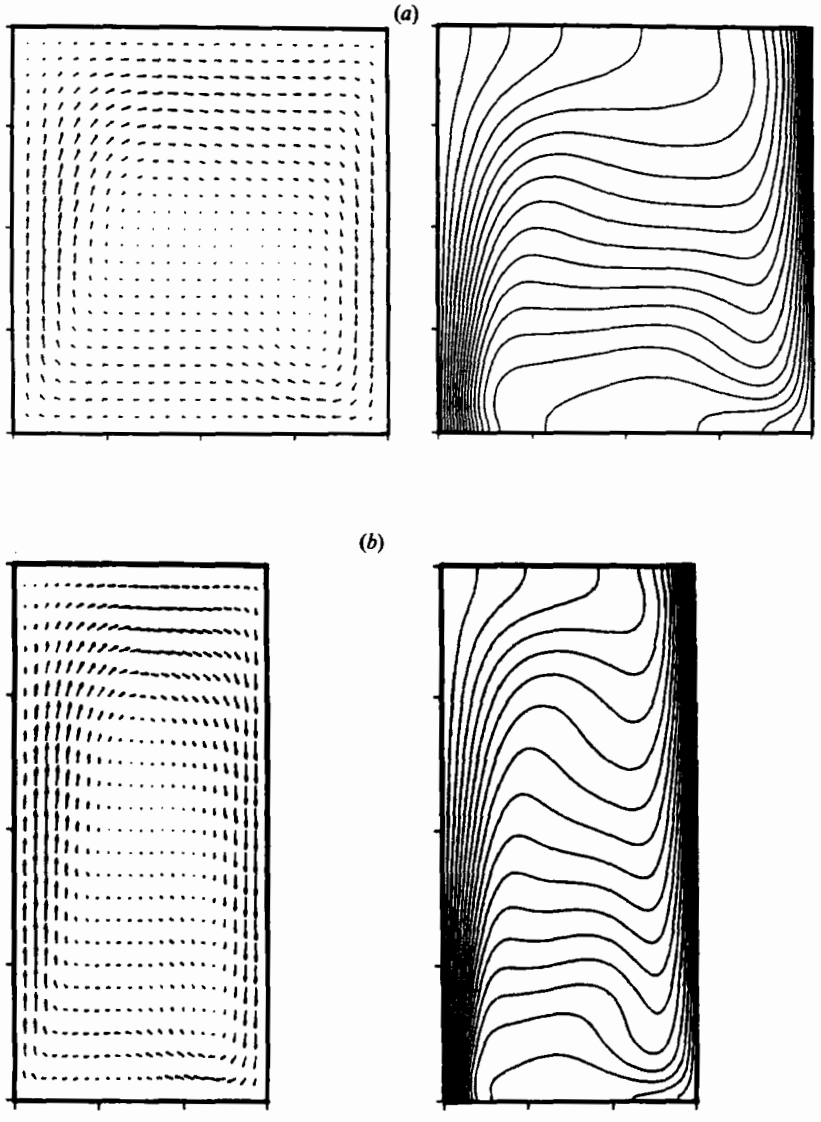

FIGURE 9(a, b). For caption see facing page.

11, where we show the results for $\epsilon \ll 1$, $Ra = 8 \times 10^7$ and $A = 1$. If the flow is highly supercritical these waves break, resulting in an unsteady disordered interface downstream. Paolucci (1986) shows that for $\epsilon \ll 1$, the flow should become highly supercritical and unsteady at $Ra = CA^{-3}$, with $C = 10^7 - 10^8$. This estimate is consistent with figure 3, where we obtain $C \approx 10^8$. For $A > 4$ the vertical walls begin to interact with the waves to the extent that the vertical-wall boundary layers become unstable before the flow becomes highly supercritical, explaining the change in slope of the line of oscillatory instability as A increases. This scenario is identical to that at the lower right corner because of the antisymmetry in the Boussinesq limit. In the non-Boussinesq case, the cold-wall boundary layer is always thinner than that at the hot wall. For $\epsilon = 0.6$ the cold-wall boundary layer is much thinner than the

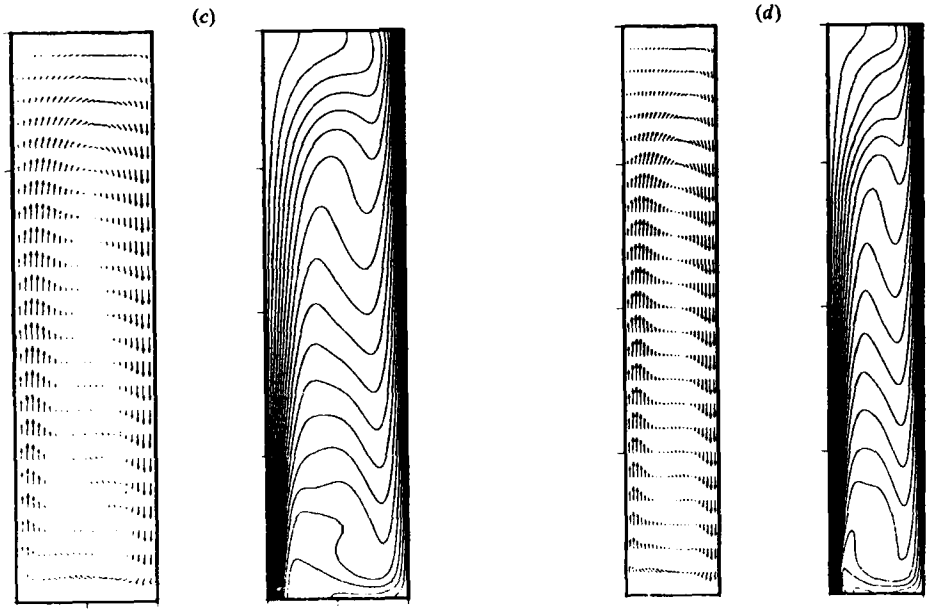

FIGURE 9. Velocity and isotherm fields for $\epsilon = 0.6$ and $Ra = 10^5$ with A as the parameter; (*a*) $A = 1$, (*b*) $A = 2$, (*c*) $A = 4$, (*d*) $A = 6$.

corresponding one for the Boussinesq case, and always becomes unstable before the internal Froude number becomes highly supercritical. This result explains the strong dependence on ϵ of the slope of the line of oscillatory instability at low aspect ratios to a slope of $A^{-1.7}$.

In the independent boundary-layer region, a nearly linear vertical thermal stratification exists in the core of the cavity (see figures 7–9, 11). The vertical temperature stratification parameter,

$$\theta A = \left(\frac{A}{2\epsilon}\right)\left(\frac{\mathrm{d}T}{\mathrm{d}y}\right)_{x=\frac{1}{2}}, \tag{8.9}$$

is given versus Ra in figure 12(*a*) for $A = 1$ and 2, and $\epsilon = 0.005$, 0.2, 0.4 and 0.6. To remove any ambiguity in the definition of θA due to temperature nonlinearities, the slope of the temperature at $y = \frac{1}{2}A$ was used to evaluate (8.9). In figure 12(*a*) it can be seen that although $0.4 < \theta A < 1.0$ when $Ra = 10^3$, θA rapidly approaches unity for larger Ra values. Also notice that little ϵ dependence exists for $Ra \geqslant 10^4$, and that which is present at $Ra = 10^3$ shows opposite trends for $A = 1$ and 2. This effect is related to the maximum in heat transfer occurring between $A = 1$ and 2 (see (7.3) and (8.10) below). Additional results of θA for $A = 1$, 2, 3, 5 and 10 are shown on figure 12(*b*) for $\epsilon = 0.005$ and $\epsilon = 0.6$, showing also that ϵ does not significantly affect θA at any aspect ratio or Ra value contained in the independent boundary-layer region (5.1) and (5.2*a*, *b*). The results on figures 12(*a*) and (*b*) agree well with the large body of similar Boussinesq results previously reported (De Vahl Davis 1968; Duxbury 1979; Eckert & Carlson 1961; Elder 1966; Raithby & Wong 1981; Roux *et al.* 1978). We note here that for $A \geqslant 4$, θA correlates with $RaA^{-\frac{5}{4}}$ and for $RaA^{-\frac{5}{4}} \geqslant 500$ is nearly constant (Duxbury 1979; Roux *et al.* 1980).

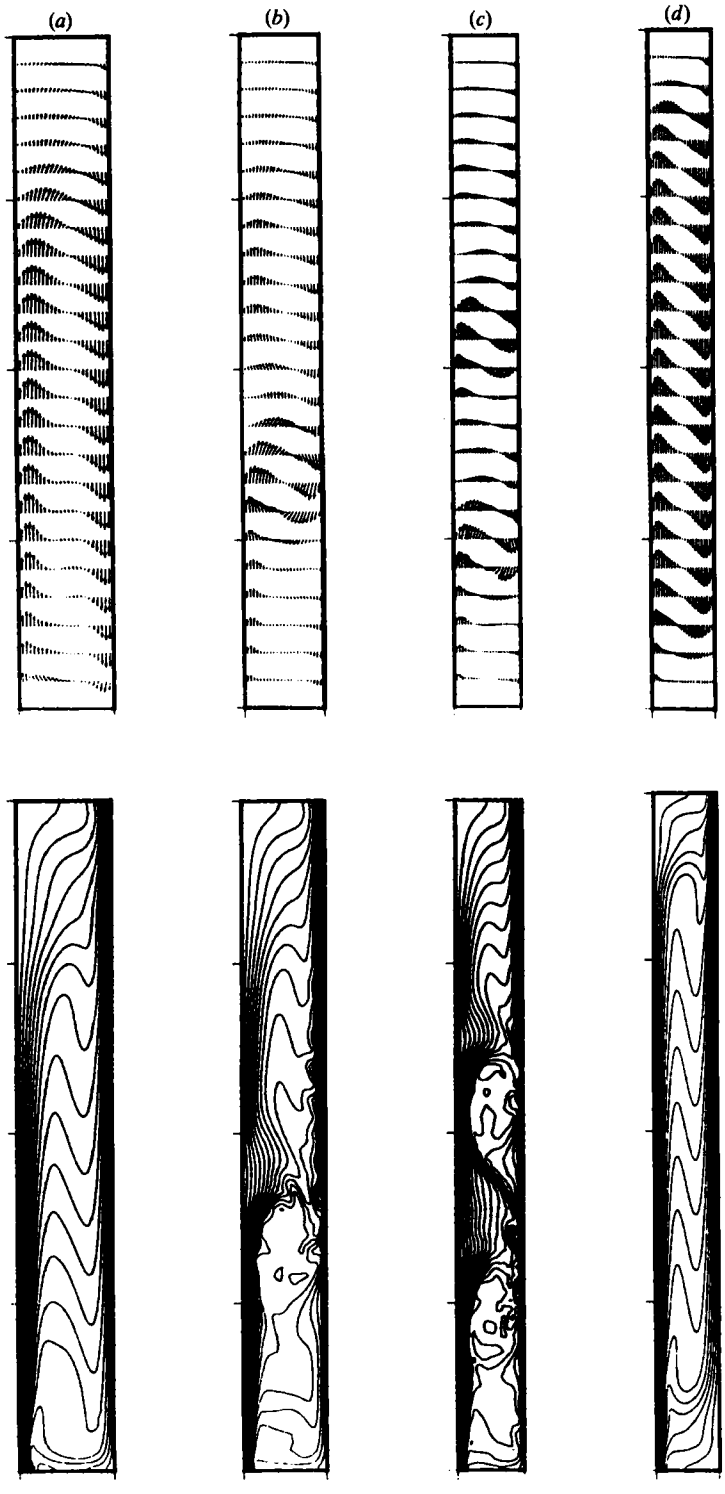

FIGURE 10. Velocity and isotherm fields for $Ra = 10^5$ showing ϵ and A effects; (*a*) $\epsilon = 0.6$, $A = 7$, (*b*) $\epsilon = 0.6$, $A = 8$, (*c*) $\epsilon = 0.6$, $A = 10$, (*d*) $\epsilon = 0.005$, $A = 10$.

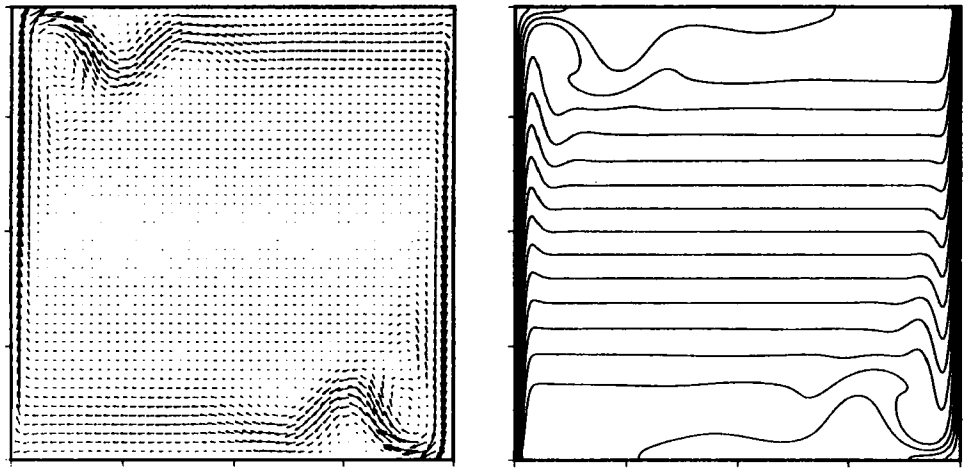

FIGURE 11. Velocity and isotherm fields for $\epsilon = 0.005$, $A = 1$, and $Ra = 8 \times 10^7$.

8.2. *Nusselt number and pressure correlations*

The Nusselt-number results shown in figure 13 can be adequately correlated for $Ra \geqslant 10^3$ by a power-law expression of the form

$$Nu_{\mathrm{b}} = \frac{\bar{Q}_{\mathrm{b}}}{Q_{\mathrm{c}}} = aRa^{b}. \tag{8.10}$$

Here the a and b depend on aspect ratio A and are nearly independent of ϵ, so that only Q_{c} accounts for the ϵ dependence of $\bar{Q}_{\mathrm{b}}$. The results for $1 \leqslant A \leqslant 5$ are correlated by the values of a and b shown in table 4 with a correlation coefficient $r = 0.9997$, although (8.10) is valid but less accurate for A well outside this range.

In the interacting and independent boundary-layer regions for $Ra \geqslant 10^3$ and satisfying (5.1), the results can be described by the expressions

$$a = 0.324A^{-\frac{1}{4}}(1-nA^{-n})^{n} \quad (n = 0.7), \tag{8.11}$$

$$b = 0.05(5+A^{-1}), \tag{8.12}$$

with a maximum error of $\pm 3.5\%$.

The pressures shown in figures 14 and 15 have a more complicated behaviour than the Nusselt numbers; they start from a plateau at low Ra, and near $Ra = 10^3$ they fall rapidly with increasing Ra until a minimum is reached, and then at large Ra they return to another plateau that is lower than the original one by an amount depending on ϵ. This complicated behaviour can be described for $Ra \geqslant 10^3$ by the expression

$$\bar{p}_{\mathrm{b}}/\bar{p}_{\mathrm{c}} = \{1-\Delta Y \exp[B(X_{\mathrm{F}}-X)^{N}(X-X_0)]\}, \tag{8.13}$$

where

$$X = \log_{10} Ra, \tag{8.14}$$

and

$$N = \left(\frac{X_{\mathrm{F}}-X_{\mathrm{M}}}{X_{\mathrm{M}}-X_0}\right). \tag{8.15}$$

Here X_0 is the value of X where the final pressure level is first crossed during the fall to the pressure minimum which is reached at X_{M}. The final pressure level is

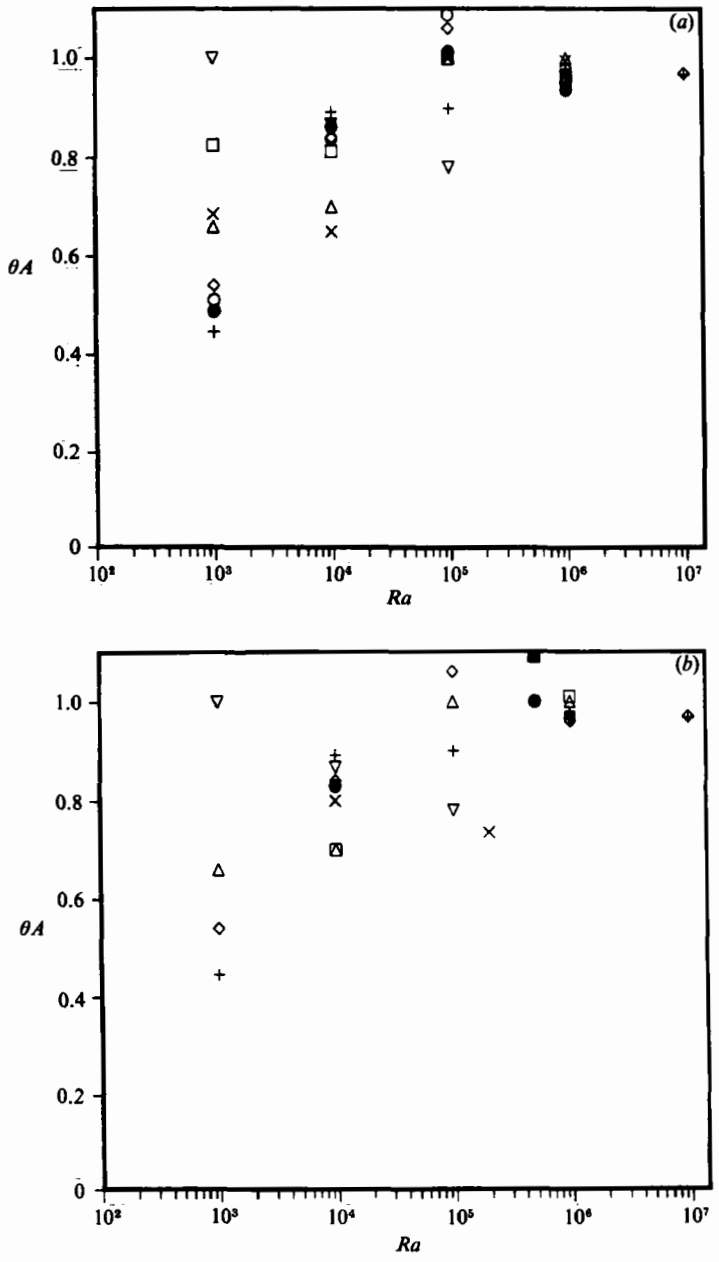

FIGURE 12. Vertical temperature stratification parameter θA versus Ra. (*a*) $A = 1$: $\diamond$, $\epsilon = 0.005$; $\odot$, $\epsilon = 0.2$; $\bullet$, $\epsilon = 0.4$; $+$, $\epsilon = 0.6$. $A = 2$: $\triangle$, $\epsilon = 0.005$; $\times$, $\epsilon = 0.2$; $\square$, $\epsilon = 0.4$; $\triangledown$, $\epsilon = 0.6$. (*b*) $\epsilon = 0.005$: $\diamond$, $A = 1$; $\triangle$, $A = 2$; $\square$, $A = 3$; $\bullet$, $A = 5$; $\times$, $A = 10$. $\epsilon = 0.6$: $+$, $A = 1$; $\triangledown$, $A = 2$; $\odot$, $A = 3$; $\blacksquare$, $A = 5$.

approached near $X_F \approx 7$. For large aspect ratios the minimum pressure and the final plateau cannot be reached within the laminar boundary-layer region, but for the region under consideration here the functions

$$N = \frac{3}{2} - \frac{0.23}{A} + \frac{6.73}{A^8} \tag{8.16}$$

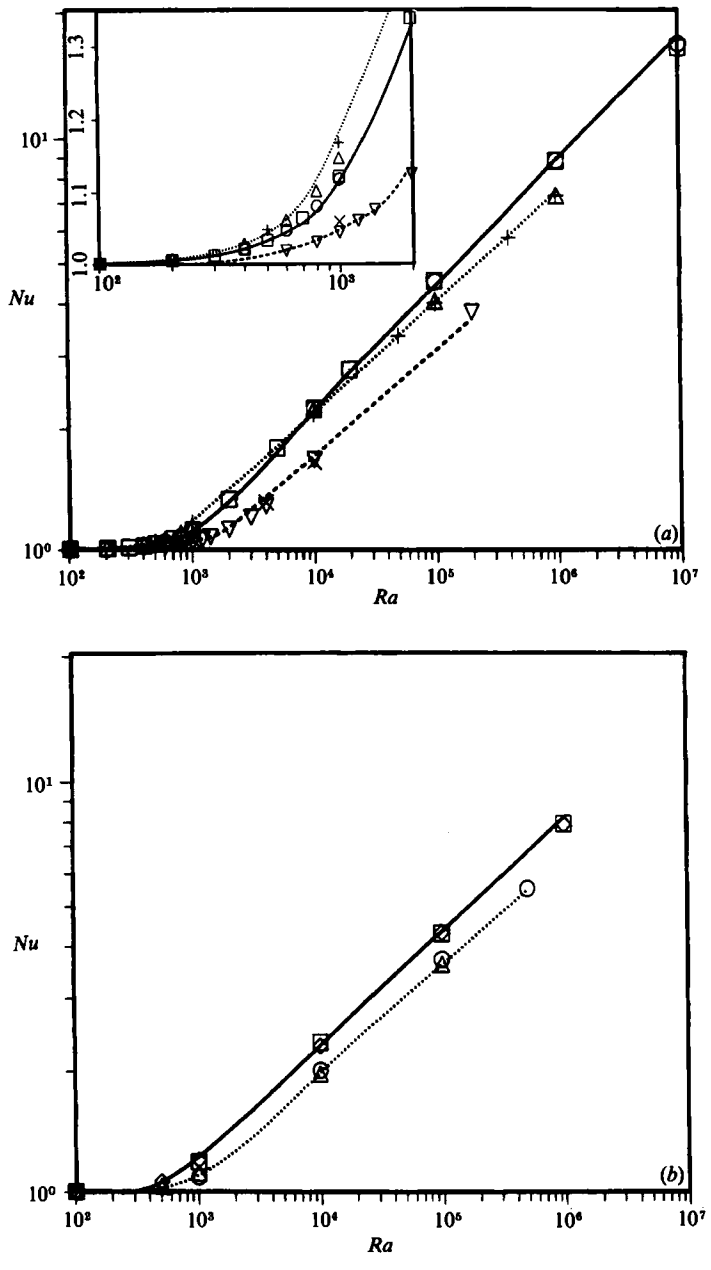

FIGURE 13. *Nu* versus *Ra* and A and ϵ as parameters. (*a*) Numerical: $\epsilon = 0.005$: ⊙, $A = 1$; △, $A = 3$; ▽, $A = 10$. $\epsilon = 0.6$: □, $A = 1$; +, $A = 3$; ×, $A = 10$. Equation (8.21): ——, $A = 1$; · · · · · ·, $A = 3$; – – –, $A = 10$. (*b*) Numerical: $\epsilon = 0.005$: □, $A = 2$; ⊙, $A = 5$. $\epsilon = 0.6$: ◇, $A = 2$; △, $A = 5$. Equation (8.21): ——, $A = 2$; · · · · · ·, $A = 5$.

and
$$X_0 = 3.3 + 0.65 \ln A, \tag{8.17}$$

adequately describe N and X_0. The difference between the initial and final pressure plateau is described by

$$\Delta Y = (\tfrac{1}{3}\epsilon)^2, \tag{8.18}$$

A	a	b
1	0.1448	0.2969
2	0.1853	0.2727
3	0.1880	0.2657
5	0.1803	0.2615

TABLE 4. Values of the parameters a and b in equation (8.10) as functions of aspect ratio.

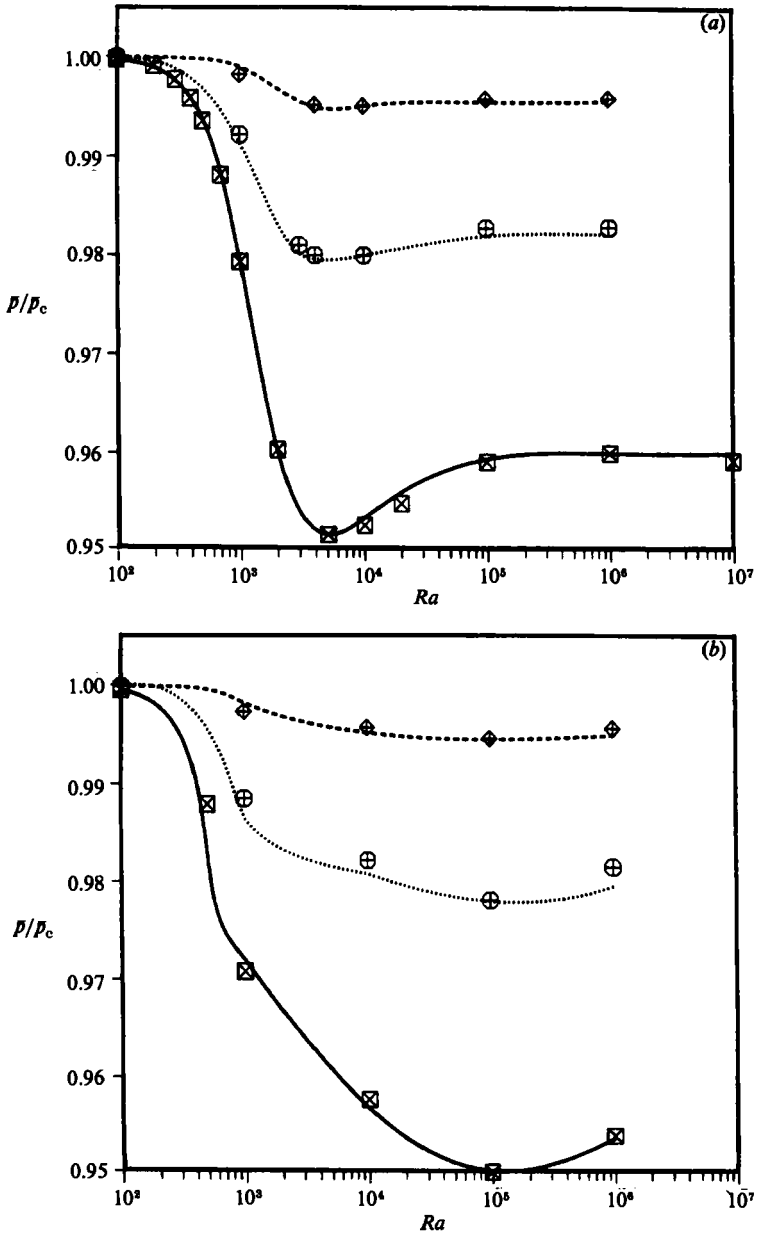

FIGURE 14. $\bar{p}/\bar{p}_c$ versus Ra; (a) $A = 1$, (b) $A = 2$. Numerical: ⊕, $\epsilon = 0.2$; ⊕, $\epsilon = 0.4$; ⊠, $\epsilon = 0.6$. Equation (8.22): - - -, $\epsilon = 0.2$; · · ·, $\epsilon = 0.4$; ——, $\epsilon = 0.6$.

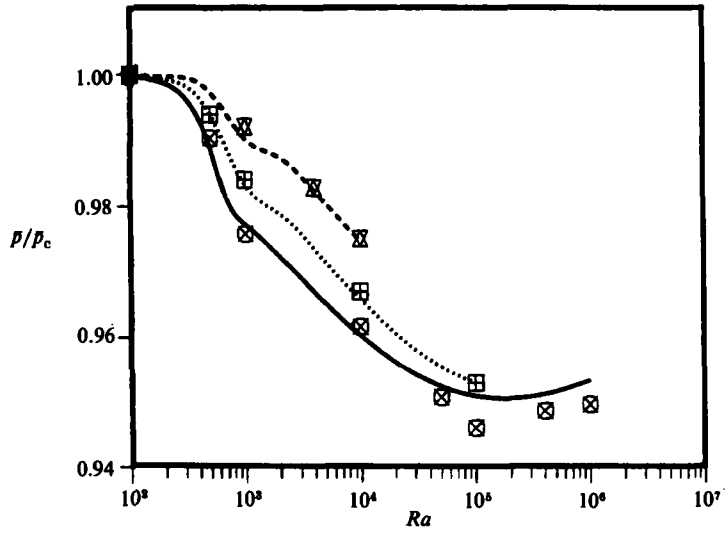

FIGURE 15. $\bar{p}/\bar{p}_c$ versus Ra for $\epsilon = 0.6$. Numerical: ⊠, $A = 3$; ⊞, $A = 5$; ⊠, $A = 10$. Equation (8.22): ——, $A = 3$; · · ·, $A = 5$; – – –, $A = 10$.

and the rate of change between the pressure levels can be specified by

$$B = B_0\left[1+2.62\left(\frac{\epsilon}{A}\right)^3\right], \tag{8.19}$$

where

$$B_0 = 2.20\times10^{-5}+\frac{6.28\times10^{-2}(A-1)^{L+0.26}}{(A-1)^L+L\times10^{-3}}. \tag{8.20}$$

The value of $L = 4$ gives the proper behaviour for all $A \geqslant 1$. Although (8.16), (8.19) and (8.20) have a complex A and ϵ dependence, notice that for $A \geqslant 3$, B becomes independent of ϵ and is in fact only a simple power law, where $B \approx B_0 \approx 0.063(A-1)^{0.26}$ results. Similarly the A^{-8} term in (8.16) becomes negligible for $A \geqslant 3$ so that most of the aspect ratio complexity is confined to the region $1 \leqslant A \leqslant 3$ as it was for the Nusselt number; note that for $A \geqslant 2$, N is almost constant over a wide range of A ($1.41 \leqslant N \leqslant 1.5$). The expressions (8.13)–(8.20) correlate the pressure results to within $\pm 0.05\,\%$ error. The maximum pressure change is about 6 % total when $\epsilon \leqslant 0.6$, where the Nusselt number varies from unity to values as large as 18. Although the total pressure variation (required for mass conservation) is small, any inaccuracy in its computation would result in much larger errors in velocity. This fact is best illustrated by looking at the analytical solution in the fully developed merged region.

8.3. *Nusselt number and pressure correlations in the combined regions*

The Nusselt number, given by (8.10), approaches zero as the Rayleigh number approaches zero. Since the correct limiting behaviour is given by expression (7.3), it is desirable to determine a single expression for Nu valid over the entire stable laminar Ra range described at the beginning of this section.

This can be done without much loss in accuracy for $Nu-1$ if the Nusselt number has the form

$$Nu = \frac{\bar{Q}}{\bar{Q}_c} = Nu_b+(Nu_n-Nu_b)\exp\left[-5\times10^2(Nu_n-1)^3\right], \tag{8.21}$$

which is simply a blending of functions (7.3) and (8.10) across $5 \times 10^2 \leqslant Ra \leqslant 10^3$, and Q_c is given by (7.1). Clearly this expression has the correct asymptotic behaviour for small Ra because this is included properly in Nu_n and it extends up to the point where unsteady motion first occurs via Nu_b. The lines in figures 13(*a*) and (*b*) show (8.21) compared to specific numerical results for $A = 1, 2, 3, 5$ and 10 with $\epsilon = 0.005$ and 0.6. As apparent from these figures, the Nu dependence on ϵ is negligible.

The analogous expression to (8.21) for $\bar{p}$ over the same region is given by

$$\bar{p} = \bar{p}_b + (\bar{p}_n - \bar{p}_b) \exp\left[-4 \times 10^3 \left(1 - \frac{\bar{p}_n}{\bar{p}_c}\right)^2\right], \tag{8.22}$$

in terms of $\bar{p}_c$, $\bar{p}_n$ and $\bar{p}_b$ given by (7.2), (7.4) and (8.13) respectively. This expression is compared with specific numerical results for $\epsilon = 0.2$, 0.4 and 0.6 for $A = 1$ and 2, on figures 14(*a*) and (*b*), respectively. Similarly figure 15 gives results for $A = 3$, 5 and 10 with $\epsilon = 0.6$. As can be observed from these figures, the Rayleigh number at which the minimum pressure is obtained is only a function of aspect ratio and can be obtained from (8.14)–(8.17).

9. Comparison of results

A more thorough comparison of the present results with other published data is given in this section.

9.1. *Flow regions*

Varying amounts of theoretical and experimental information relating to flow-region classification in the Boussinesq limit and near-Boussinesq limit can be found in Batchelor (1954), Bergholz (1978), Duxbury (1979), Eckert & Carlson (1961), Lauriat (1980), Lee & Korpela (1983), Mordchelles-Regnier & Kaplan (1963), Polezhaev (1968), and Yin, Wung & Chen (1978). Much of the difference in the flow-region bounds can often be related to the use of different criteria for the classification, although in some cases poor numerical resolution or experimental difficulties are responsible for the differences. A somewhat different picture will emerge if velocity field rather than thermal field or heat transfer information is used. Here the velocity field behaviour was used to construct figure 3, as was previously described. In general the results on figure 3 agree better with the published literature in the region $A < 12$ than for the higher aspect ratios.

Our location of the unsteady transition, displayed in figure 3, is defined by the upper limit of (5.2*a*). The results of Mordchelles-Regnier & Kaplan (1963), for $A < 12$ and extending down to aspect ratios as low as 1.67, predict that the critical Rayleigh number varies with $A^{-0.5}$. Most of the disagreement with our results is at the lower aspect ratios, where we show an A^{-3} dependence. We note that as the aspect ratio is decreased, heat losses from the ends become more and more important and cause instabilities to occur at a lower value of Rayleigh number. Apparently, these end losses are responsible for their weaker dependence on aspect ratio. We have much better quantitative agreement with results obtained by linear stability analysis by Bergholtz (1978). In making this comparison we have made use of the fact that the stratification parameter, defined by (8.9), is near unity in this region. His results do show that the critical Rayleigh number varies approximately with aspect ratio as A^{-3} for $A < 6$. We note that the result obtained from Bergholtz's analysis arises from a travelling-wave instability along the sidewalls. However, we previously offered possible explanation for the A^{-3} behaviour due to a 'hydraulic'

jump instability on the endwalls. The experimental results of Ivey (1984) for $Pr = 7.1$ and $A = 1$ clearly indicate the presence of a 'hydraulic' jump and a stationary wavetrain downstream of it when the Rayleigh number is above the critical internal Froude number. His observations are in complete agreement with our results, an example of which is shown in figure 11. However, we know of no other results which show that for low A in the Boussinesq regime the instability is due to wave-breaking arising from the 'hydraulic' jump rather than the travelling-wave instability arising for larger A.

Bergholtz's (1978) results also show that there is a minimum critical Rayleigh number for oscillatory instability, occurring at 1.15×10^5 at an aspect ratio near 12. This compares well with our minimum of $Ra = 2.4 \times 10^5$ also occurring near $A = 12$. At aspect ratios larger than 12 our results show that the stratification parameter is nearer 0.5, and the critical Rayleigh number is approximately linear with A. This picture is in good agreement with the travelling-wave instability from steady to unsteady motion given by Bergholtz (1978), and consistent with experimental data of Mordchelles-Regnier & Kaplan (1963) for $12 \leqslant A \leqslant 25$.

Results of Lee & Korpela (1983), and Lauriat (1980) show that in the Boussinesq limit, for $Ra \approx 10^4$ the flow changes from unicellular to multicellular motion as the aspect ratio is increased. They observe the transition to occur near $A = 11$–12, in agreement with the minimum aspect ratio shown in figure 3.

Still in the Boussinesq regime, Bergholtz (1978) also obtained critical Rayleigh number corresponding to the standing-wave or stationary transition from fully developed merged boundary layers to steady multicellular motion. He found this value to be approximately 5740, which again compares very well with our value given by (7.5) for $\epsilon \to 0$. However, Lee & Korpela (1983), using 17 grid points in the horizontal direction, obtain this transition between 7100 and 7810 for $A = 20$, which is much higher than our and Bergholtz's results. They explain this disagreement by noting that for large but finite aspect ratios of order 20 there is a small positive vertical stratification through the cavity, since the boundary layers are not yet completely developed, and Bergholtz shows that the flow is stabilized with increasing stratification. Even though this argument correctly explains why for lower aspect ratios the critical Rayleigh number should increase, we have not observed a substantial increase until $A < 20$. In fact, our calculation for $Ra = 7100$ and $A = 20$ shows multicellular motion, in agreement with the results of Roux *et al.* (1980) obtained by using a higher-order scheme. A better explanation for the disagreement is that Lee & Korpela lacked sufficient horizontal resolution.

The lower bound on the fully developed boundary-layer region $A > Ra/500$ given by Batchelor (1954) agrees with figure 3 for large Ra but differs substantially at low Ra, since fully developed boundary layers at the mid-height plane cannot be developed for $A < 2$ even if Ra and ϵ approach zero.

Finally, Polezhaev (1968) constructed a fairly complete picture of the flow regions for the same A and Ra ranges shown on figure 3. In spite of the very coarse grids used, the regions where calculations were made and those where he used data from Eckert & Carlson (1961) as well as Elder (1965) are in qualitative agreement with figure 3. However, in the regions where he extrapolated the bounds there is substantial disagreement, particularly where both A and Ra are large and where both are small. The same statement applies to the regions plot given by Yin *et al.* (1978), since only a band of results extending from low Ra and high A to high Ra and low A were used to locate lines which were then extrapolated across the other regions.

Roux *et al.* (1980) found, in the Boussinesq limit, that a small region of reverse

transition from multicellular to unicellular flow exists within the lower right corner of the region defined by $A \geqslant 12$ and $10^4 \leqslant Ra \leqslant 10^5$. We note that this region corresponds to the narrow region separating stationary and oscillatory stability branches, for a narrow range of stratification parameter, as given in figure 3 of Bergholtz (1978). We have verified the existence of this narrow region for $\epsilon \ll 1$. However, as ϵ increases, this region quickly disappears and, as suggested by the dashed line in figure 3, this region does not exist for $\epsilon = 0.6$.

9.2. *Conduction solution*

It was previously pointed out that Chenoweth & Paolucci (1985) give the exact solution for the conduction limit ($Ra \to 0$). It was also stated that those results showed that the heat flux Q_c, as given by (7.1), is not greatly different from the constant conductivity value of -2ϵ, so that the average heat flux could be normalized by either to give the Nusselt-number results without serious error. It was also shown that the pressure level is significantly different for Sutherland-law and constant conductivity given by (7.2) and (6.7) respectively. The exact-solution results can be used to evaluate limiting results from numerical calculations. This was done in this paper. Unfortunately, Leonardi & Reizes (1979, 1981) used the pressure solution (6.7), obtained by use of constant conductivity, to explain their numerical results obtained using Sutherland-law conductivity. They expected to obtain agreement at low Ra values where they stated that linear temperature profiles should exist; of course, the temperature profiles are highly nonlinear near the cold wall with increasing ϵ, and the value of $\bar{p}_c$ given by (7.2) is very sensitive to values of conductivity there, so that the constant-conductivity result (6.7) is much lower than that obtained from the Sutherland law. Leonardi & Reizes (1979) were puzzled by the apparent better agreement of their numerical results with (6.7) for large Ra than at low Ra where it should occur. This fortuitous result is related to the linearly stratified core region with nearly uniform horizontal temperature at large Ra. We note that Leonardi & Reizes use a complicated vorticity–stream-function formulation to compute their results, and it appears that the term giving rise to the secondary source of vorticity $-\nabla\rho \times \nabla(\frac{1}{2}v^2)$ was not correctly given in their equations. This error does not appear in Leonardi & Reizes (1981). There, using some irrelevant scaling changes (to be discussed shortly), they stated that good agreement was obtained between numerical results and (6.7) over the entire Ra range. As shown earlier, the numerical results obtained here do asymptotically approach the proper exact solution as $Ra \to 0$, rather than the much lower result (6.7), for all ϵ provided a sufficient number of grid points are used to give the resolution required. It does not appear, however, that the results of Leonardi & Reizes (1979, 1981) at low Ra approach either (6.7) or the exact solution (7.2).

9.3. *Near-conduction results*

Batchelor (1954) estimated that in the Boussinesq limit for large A and small Ra

$$Nu_n - 1 \approx 10^{-8} \frac{Ra^2}{A}, \tag{9.1}$$

which he believed to be valid for $Ra \leqslant 10^3$. Later Poots (1958) used numerical calculations for $\epsilon \ll 1$, $A = 1$ and $Ra = 5 \times 10^2$ and 10^3 to show that

$$Nu_n - 1 \approx 5 \times 10^{-8} Ra^2, \tag{9.2}$$

for $Ra \leqslant 10^3$. More recently Roux *et al.* (1978) used more accurate numerical results for $\epsilon \ll 1$, $A = 1$ and $Ra = 10^2, 5 \times 10^2$ and 10^3 and state that they 'agree with' Poots'

results. Actually there is substantial difference between the results of Poots and Roux *et al.*, so that the corroboration is not justified. In fact, the data of Roux *et al.* agree better with (7.3) than with (9.2). For $A = 1$, (7.3) gives

$$Nu_n - 1 \approx 1.46 \times 10^{-7} Ra^2, \tag{9.3}$$

and for $A \gg 1$, it yields

$$Nu_n - 1 \approx 5.84 \times 10^{-7} \frac{Ra^2}{A}, \tag{9.4}$$

so that the constant of proportionality is not only highly dependent on A but is also much larger than has previously been reported. This is due to the fact that accurate results for several points with $Ra \leqslant 500$ must be used to determine the constant for each value of A.

9.4. *Boundary-layer region*

The present results have already been validated for large ϵ using results from exact solutions in the conduction limit and in the fully developed merged boundary-layer regime, as well as the established Boussinesq limit in the boundary-layer region. Here some additional discussion of the effects of ϵ on the results is given.

The only known data for ϵ as large as 0.6 and $10^3 \leqslant Ra \leqslant 10^6$ which can be compared with the present results are those of Leonardi & Reizes (1979, 1981). Their steady-state results were obtained by means of a false-transient method for solving the Navier–Stokes equations using a vorticity–stream-function formulation. Their earlier results for Nu showed considerable ϵ dependence (as much as 33 % at large Ra) as ϵ varied from the Boussinesq limit 0.0018 up to 0.6. Their later paper showed only 10 % dependence for $0.005 \leqslant \epsilon \leqslant 0.5$ on a much reduced Ra range. The reason for the ϵ dependence in either their earlier or later work is not clear, since the present results in figure 13 show little or no ϵ-dependence. Only about 2 % of the difference can be attributed to their use of the constant-property conduction heat flux to normalize their average heat flux obtained with Sutherland-law properties.

The pressure levels given by Leonardi & Reizes (1979) for $A = 2$ consistently fall much lower than those reported here on figure 14. In many cases they reported a pressure drop approximately a factor of two larger than is obtained here. We do not have an explanation for this discrepancy. There is certainly a question regarding the lack of resolution present for the coarse (17×17) and (33×33) uniform grids used to produce their results for similar parameter values where (81×81) were found to be necessary here. Unfortunately, lack of resolution in the present results produced pressures even higher than those shown on figures 14 and 15. Just as puzzling are their later pressure-level results for $A = 1$, where good agreement with (6.7) is obtained for all Ra and all ϵ, even though (6.7) is valid only for low Ra and constant conductivity rather than the Sutherland-law variation they used; it also appears that the definitions of $\bar{p}$, Ra, and ϵ used there were altered due to an unimportant but confusing change of the reference temperature from the average $\frac{1}{2}(T_h + T_c)$, as is used here and in their earlier paper, to the cold wall value T_c. This change in reference-temperature definition makes their later results for $\bar{p}$ greater than unity, and Ra and ϵ values appear to be larger than the equivalent values given in their earlier paper. The most plausible explanation for the Nu and $\bar{p}$ discrepancies between their results and ours involves the possibility that their results had not yet reached steady state. This is possible since they apparently used only the criterion that the average hot- and cold-wall Nusselt numbers be approximately equal to indicate steady state. We

have found that this criterion must be supplemented by the additional condition $\bar{p} \neq \bar{p}(t)$ for large ϵ. That is, usually the hot- and cold-wall Nu values became approximately equal and then drifted together to their final value while the pressure adjusted on a much longer timescale to its final steady-state level. In fact we have found that steady state was approximately achieved when the non-dimensional time obeyed the following empirical inequality:

$$t > \frac{2\pi(1+2\epsilon)^{\frac{1}{4}}}{\pi + A^{-0.1}Ra^{\frac{1}{4}}}. \tag{9.5}$$

Note that the Rayleigh-number dependence in (9.5) is the same as that given by Patterson & Imberger (1980), who used scaling arguments to predict when the flow reaches steady state; however, our aspect-ratio dependence is weaker than theirs since they show that it varies as $A^{\frac{1}{4}}$. The difference in the aspect-ratio dependence may be attributable to the fact that in the scaling analysis the fluid entrained by the boundary layers is assumed unstratified. Clearly, the error in this assumption increases with time. We point out that calculations near the critical Rayleigh numbers to unsteady flow require times much larger than that given by (9.5) in order to observe whether small perturbations decay or amplify.

As noted by Eckert & Carlson (1961) and Elder (1965), among others, the non-interacting boundary layers in a slot grow similar to that of a single flat plate. Following Eckert & Carlson, if the assumption is made that the boundary layers are locally similar, and if we take the stratification parameter $\theta A = 1$ (see (8.9)), then the heat transfer can be obtained approximately by using the similar solution given by Hara (1958), and independently by Sparrow & Gregg (1958), for laminar flow of air on a vertical flat plate with large temperature difference. To that end, if the linear temperature profile in the middle of the slot, obtained from (6.14), is introduced into Hara's Nusselt-number variation, we can compute the average heat transfer in the slot. The result is

$$Nu_{\mathrm{b}} = -0.272\left(\frac{Ra}{A}\right)^{\frac{1}{4}}\frac{2\epsilon}{Q_{\mathrm{c}}}(1-0.0825\epsilon), \tag{9.6}$$

where Q_{c} is given by (7.1). We note that in obtaining (9.6) end effects have not been properly accounted for since the linear stratification was assumed to hold over the whole height of the cavity. Nevertheless, heat-transfer results obtained from (8.10) and (9.6) differ by at most 20 % over the entire boundary-layer regime. The important conclusion that can be drawn from (9.6) is that results for $\epsilon = 0$ and 0.6 differ by only 3 %. If a more realistic value of $\theta A < 1$ had been used, the ϵ dependence would be weaker, and it would be weaker still if the slightly different similarity solution obtained by Sparrow & Gregg had been used, since by using a different procedure to Hara, they obtain a slightly weaker ϵ-dependence. Equation (9.6) thus supports our conclusion that any ϵ-dependence in heat transfer is very weak.

10. Conclusions

The numerical solutions to the Navier–Stokes equations given here contribute to the physical understanding of a classical convection problem for a broad range of parameters. The solutions were validated by means of limiting exact solutions as well as the vast body of literature on the well-established Boussinesq limit.

Although the average Nusselt number (defined using the proper conduction solution) is almost independent of the temperature-difference parameter, the velocity

and temperature fields as well as the pressure level show significant dependence on this parameter. The total pressure variation in all cases is small; however, any inaccuracy in its computation, arising from lack of mass conservation, results in much larger errors in velocity. It also appears that the critical Rayleigh numbers for stationary and oscillatory instabilities are lowered with increasing temperature difference. In addition we observe that in some cases the physical nature of the instability is different. This is an area where further investigation is needed. It is clear that there can be considerable risk if results obtained from the well-established Boussinesq limit are extrapolated for use where large temperature differences exist.

REFERENCES

ADAMS, J. C., SWARZTRAUBER, P. N. & SWEET, R. A. 1981 Efficient fortran subprograms for the solution of elliptic partial differential equations. In *Elliptic Problem Solvers* (ed. M. H. Schultz), pp. 187–190. Academic Press.

BATCHELOR, G. K. 1954 Heat transfer by free convection across a closed cavity between vertical boundaries at different temperatures. *Q. Appl. Maths* **12**, 209–233.

BERGHOLZ, R. F. 1978 Instability of steady natural convection in a vertical fluid layer. *J. Fluid Mech.* **84**, 743–768.

CHENOWETH, D. R. & PAOLUCCI, S. 1985 Gas flow in vertical slots with large horizontal temperature differences. *Phys. Fluids* **28**, 2365–2374.

CHENOWETH, D. R. & PAOLUCCI, S. 1986 Transient natural convection in vertical slots with large temperature differences, in preparation.

DE VAHL DAVIS, G. 1968 Laminar natural convection in an enclosed rectangular cavity. *Intl J. Heat Mass Transfer* **11**, 1675–1693.

DE VAHL DAVIS, G. 1983 Natural convection of air in a square cavity: a bench mark numerical solution. *Intl J. Numer. Meth. Fluids* **3**, 249–264.

DE VAHL DAVIS, G. & JONES, I. P. 1983 Natural convection in a square cavity: a comparison exercise. *Intl J. Numer. Meth. Fluids* **3**, 227–248.

DUXBURY, D. 1979 An interferometric study of natural convection in enclosed plane air layers with complete and partial central vertical divisions. Ph.D. thesis, University of Salford, U.K.

ECKERT, E. R. G. & CARLSON, W. O. 1961 Natural convection in an air layer enclosed between two vertical plates with different temperatures. *Intl J. Heat Mass Transfer* **2**, 106–120.

ELDER, J. W. 1965 Laminar free convection in a vertical slot. *J. Fluid Mech.* **23**, 77–98.

ELDER, J. W. 1966 Numerical experiments with free convection in a vertical slot. *J. Fluid Mech.* **24**, 823–843.

GILL, A. E. 1966 The boundary layer regime for convection in a rectangular cavity. *J. Fluid Mech.* **26**, 515–536.

HARA, T. 1958 Heat transfer by laminar free convection about a vertical flat plate with large temperature difference. *Bull. JSME* **1**, 251–254.

HARLOW, F. H. & WELCH, J. E. 1965 Numerical calculation of time-dependent viscous incompressible flow of fluid with free surface. *Phys. Fluids* **8**, 2182–2189.

HILSENRATH, J., BECKETT, C. W., BENEDICT, W. S., FANO, L., HODGE, H. J., MASI, J. F., NUTTALL, R. L., TOULOUKIAN, Y. S. & WOOLLEY, H. W. 1960 *Tables of Thermodynamic and Transport Properties*. Pergamon.

HINDMARSH, A. C., GRESHO, P. M. & GRIFFITHS, D. F. 1984 The stability of explicit Euler time-integration for certain finite difference approximations of the multi-dimensional advection–diffusion equation. *Intl J. Numer. Meth. Fluids* **4**, 853–897.

HIRT, C. W. & HARLOW, F. H. 1967 A general corrective procedure for the numerical solution of initial-value problems. *J. Comp. Phys.* **2**, 114–119.

IVEY, G. N. 1984 Experiments on transient natural convection in a cavity. *J. Fluid Mech.* **144**, 389–401.

LAURIAT, G. 1980 Numerical study of natural convection in a narrow vertical cavity: an examination of high-order accuracy schemes. *ASME-AICHE Heat Transfer Conference, Orlando, Florida, July 1980, ASME Paper No.* 80-HT-90.

LEE, Y. & KORPELA, S. A. 1983 Multicellular natural convection in a vertical slot. *J. Fluid Mech.* **126**, 91–121.

LEONARDI, E. & REIZES, J. A. 1979 Natural convection in compressible fluids with variable properties. In *Numerical Methods in Thermal Problems* (ed. R. W. Lewis & K. Morgan), pp. 297–306. Swansea: Pineridge Press.

LEONARDI, E. & REIZES, J. A. 1981 Convective flows in closed cavities with variable fluid properties. In *Numerical Methods in Heat Transfer* (ed. R. W. Lewis, K. Morgan & O. C. Zienkiewicz), pp. 387–412. John Wiley.

LE QUERE, P. & ALZIARY DE ROQUEFORT, T. 1985 Computation of natural convection in two-dimensional cavities with Chebyshev polynomials. *J. Comp. Phys.* **57**, 210–228.

MALLINSON, G. D. & DE VAHL DAVIS, G. 1977 Three-dimensional natural convection in a box: a numerical study. *J. Fluid Mech.* **83**, 1–31.

MORDCHELLES-REGNIER, G. & KAPLAN, C. 1963 Visualization of natural convection on a plane wall and in a vertical gap by differential interferometry. Transitional and turbulent regimes. In *Heat Transfer Fluid Mech. Inst.*, pp. 94–111. Stanford University Press.

PAOLUCCI, S. 1982 On the filtering of sound from the Navier–Stokes equations. *Sandia National Laboratories Rep.* SAND82-8257 December.

PAOLUCCI, S. 1986 Direct numerical simulation of turbulent natural convection in an enclosed cavity. To be published.

PATTERSON, J. & IMBERGER, J. 1980 Unsteady natural convection in a rectangular cavity. *J. Fluid Mech.* **100**, 65–86.

POLEZHAEV, V. I. 1967 Numerical solution of a system of two-dimensional unsteady Navier–Stokes equations for a compressible gas in a closed region. *Fluid Dyn.* **2**, 70–74.

POLEZHAEV, V. I. 1968 Flow and heat transfer in laminar natural convection in a vertical layer. *Teplo i Massoobmen* **1**, 631–640.

POOTS, G. 1958 Heat transfer by laminar free convection in enclosed plane gas layers. *Q. J. Mech. Appl. Maths* **11**, 257–273.

RAITHBY, G. D. & WONG, H. H. 1981 Heat transfer by natural convection across vertical air layers. *Numer. Heat Transfer* **4**, 447–457.

ROUX, B., GRONDIN, J. C., BONTOUX, P. & DE VAHL DAVIS, G. 1980 Reverse transition from multicellular to monocellular motion in vertical fluid layer. *Physico Chemical Hydrodynamics.* Madrid: European Physical Society.

ROUX, B., GRONDIN, J. C., BONTOUX, P. & GILLY, B. 1978 On a high-order accurate method for the numerical study of natural convection in a vertical square cavity. *Numer. Heat Transfer* **1**, 331–349.

RUBEL, A. & LANDIS, F. 1970 Laminar natural convection in a rectangular enclosure with moderately large temperature differences. *Heat Transfer 1970* **4**, NC2.10, pp. 1–11. Dusseldorf: VDI.

SCHINKEL, W. M. M., LINTHORST, S. J. M. & HOOGENDOORN, C. J. 1980 The stratification in natural convection in vertical enclosures. *Proc. 19th ASME–AICHE Natl Heat Transfer Conf. Natural Convection in Enclosures.* Orlando, Florida.

SPARROW, E. M. & GREGG, J. L. 1958 The variable fluid-property problem in free convection. *Trans. ASME* **80**, 879–886.

WHITE, F. M. 1974 *Viscous Fluid Flow*, pp. 29–32. McGraw-Hill.

WILLIAMS, G. P. 1969 Numerical integration of the three-dimensional Navier–Stokes equations for incompressible flow. *J. Fluid Mech.* **37**, 727–750.

YIN, S. H., WUNG, T. Y. & CHEN, K. 1978 Natural convection in an air layer enclosed within rectangular cavities. *Intl J. Heat Mass Transfer* **21**, 307–315.